



LAWRENCE
LIVERMORE
NATIONAL
LABORATORY

Hydrogen Outgassing from Lithium Hydride

L. N. Dinh, M. A. Schildbach, R. A. Smith, B.
Balazs¹, W. McLean II

April 26, 2006

Nuclear Materials Research Developments

Disclaimer

This document was prepared as an account of work sponsored by an agency of the United States government. Neither the United States government nor Lawrence Livermore National Security, LLC, nor any of their employees makes any warranty, expressed or implied, or assumes any legal liability or responsibility for the accuracy, completeness, or usefulness of any information, apparatus, product, or process disclosed, or represents that its use would not infringe privately owned rights. Reference herein to any specific commercial product, process, or service by trade name, trademark, manufacturer, or otherwise does not necessarily constitute or imply its endorsement, recommendation, or favoring by the United States government or Lawrence Livermore National Security, LLC. The views and opinions of authors expressed herein do not necessarily state or reflect those of the United States government or Lawrence Livermore National Security, LLC, and shall not be used for advertising or product endorsement purposes.



LAWRENCE
LIVERMORE
NATIONAL
LABORATORY

UCRL-BOOK-220900

Hydrogen Outgassing From Lithium Hydride

L. N. Dinh¹, M. A. Schildbach¹, R. A. Smith², D. M.
Grant³, B. Balazs¹, W. McLean II¹

¹Lawrence Livermore National Laboratory,
Livermore, CA, USA

²BWXT-Y-12, Oak Ridge, TN, USA

³AWE, Aldermaston, UK

05/31/2006

To be submitted to the Nova Publishers as a possible
chapter in a book titled “New Research in Nuclear Materials”

This document was prepared as an account of work sponsored by an agency of the United States Government. Neither the United States Government nor the University of California nor any of their employees, makes any warranty, express or implied, or assumes any legal liability or responsibility for the accuracy, completeness, or usefulness of any information, apparatus, product, or process disclosed, or represents that its use would not infringe privately owned rights. Reference herein to any specific commercial product, process, or service by trade name, trademark, manufacturer, or otherwise, does not necessarily constitute or imply its endorsement, recommendation, or favoring by the United States Government or the University of California. The views and opinions of authors expressed herein do not necessarily state or reflect those of the United States Government or the University of California, and shall not be used for advertising or product endorsement purposes.

Hydrogen Outgassing From Lithium Hydride

L. N. Dinh¹, M. A. Schildbach¹, R. A. Smith², D. M. Grant³, B. Balazs¹, W. McLean II¹

¹Lawrence Livermore National Laboratory, Livermore, CA, USA

²BWXT-Y-12, Oak Ridge, TN, USA

³AWE, Aldermaston, UK

ABSTRACT

Lithium hydride is a nuclear material with a great affinity for moisture. As a result of exposure to water vapor during machining, transportation, storage and assembly, a corrosion layer (oxide and/or hydroxide) always forms on the surface of lithium hydride resulting in the release of hydrogen gas. Thermodynamically, lithium hydride, lithium oxide and lithium hydroxide are all stable. However, lithium hydroxides formed near the lithium hydride substrate (interface hydroxide) and near the sample/vacuum interface (surface hydroxide) are much less thermally stable than their bulk counterpart. In a dry environment, the interface/surface hydroxides slowly degenerate over many years/decades at room temperature into lithium oxide, releasing water vapor and ultimately hydrogen gas through reaction of the water vapor with the lithium hydride substrate. This outgassing can potentially cause metal hydriding and/or compatibility issues elsewhere in the device. In this chapter, the morphology and the chemistry of the corrosion layer grown on lithium hydride (and in some cases, its isotopic cousin, lithium deuteride) as a result of exposure to moisture are investigated. The hydrogen outgassing processes associated with the formation and subsequent degeneration of this corrosion layer are described. Experimental techniques to measure the hydrogen outgassing kinetics from lithium hydride and methods employing the measured kinetics to predict hydrogen outgassing as a function of time and temperature are presented. Finally, practical procedures to mitigate the problem of hydrogen outgassing from lithium hydride are discussed.

INTRODUCTION

Lithium hydride (LiH) is widely used material in the thermonuclear, fusion and space industries [1-3]. The unique properties of LiH include high hydrogen content, high melting point, low dissociation pressure and low density [4]. LiH, however, has a high affinity for moisture. The reaction of LiH with H₂O generates hydrogen gas and heat, the effects of which may be undesirable and pose compatibility or safety issues under certain circumstances. Unfortunately, as a result of exposure to moisture during routine handling, a corrosion layer always forms on the surface of LiH. Depending on the moisture exposure level and duration, lithium oxide (Li₂O) and/or lithium hydroxide (LiOH) are formed. At exposure levels greater than 15% relative humidity (RH) at room temperature, hydrated lithium hydroxide (LiOH·H₂O) is formed [5]. Even in the absence of a H₂O source, hydrogen generation from within the LiH/Li₂O/LiOH structure has been reported [6-8].

In this chapter, the different chemical pathways through which hydrogen outgassing can occur from LiH will be described. The morphology of the corrosion layer formed on LiH (and in many cases, its isotopic cousin, LiD) under different conditions as experimentally observed by scanning electron microscopy (SEM) and atomic force microscopy (AFM) will be presented. The technique of temperature programmed reaction/decomposition (TPR), in conjunction with the isoconversional thermal analysis method, was used to measure the outgassing kinetics and will be reviewed in detail. Hydrogen outgassing prediction modeling based on the measured kinetics will be demonstrated and compared against independent experimental isothermal data for validity. Finally, techniques to mitigate the problem of unwanted hydrogen outgassing from LiH will also be discussed.

CHEMICAL PATHWAYS FOR HYDROGEN OUTGASSING FROM LiH

The overall reaction of LiH with excess water proceeds according to the following chemical equation [9]:



Fig. 1 shows the phase stability diagram for lithium, hydrogen and oxygen at 298 K. The phase stability diagram suggests that the stable product for the reaction of LiH with H₂O at room temperature and at very low moisture levels is Li₂O. At higher moisture levels, the stable product is LiOH. At 15% or higher relative humidity (RH), the stable product is LiOH·H₂O. However, the phase stability diagram only allows a LiH/Li₂O interface, a Li₂O/LiOH interface and a LiOH/LiOH·H₂O interface. Consequently, the reaction of LiH with H₂O vapor at room temperature to form LiOH·H₂O has to happen in multiple steps [10] as follows:

First, LiH reacts with water vapor to form Li₂O, establishing a LiH/Li₂O interface [10-11]:



As the Li₂O layer grows thicker, further moisture reacts with the outer layer of the oxide to form LiOH, establishing a Li₂O/LiOH interface [10]:



As the LiOH grows thicker, further moisture reacts with the outer layer of the hydroxide to form LiOH·H₂O, establishing a LiOH/LiOH·H₂O interface [10]:



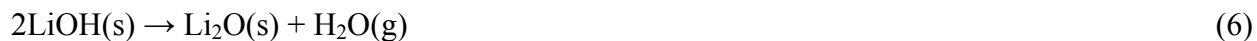
The cartoon in fig. 2 depicts the cross-sections of LiH samples that have been exposed to different moisture environments at 298K. Note the variation in the nature of the corrosion layers as a function of H₂O partial pressures. Direct and indirect experimental proofs for the Li₂O

buffer layer in between LiH and LiOH have been reported [8, 12-13], even though the exact thickness of this buffer layer has not yet been quantitatively reported in the literature.

Under most device applications (vacuum or dry environment), LiOH·H₂O is not a stable product (see the phase stability diagram in fig. 1) and decomposes into LiOH in a matter of hours [8] according to:



LiOH, in turn, decomposes slowly with time into Li₂O even at room temperature [7-8] according to:



The kinetics of the decomposition of LiOH depends on the dryness/vacuum level and temperature. It was discovered by different workers that vacuum thermal decomposition of bulk LiOH powder (grain sizes on the order of tens to hundreds of micrometers) into Li₂O follows a reaction front moving from the surface inward [8,14]. Due to stress at the LiOH/vacuum interface and defective and missing crystalline bonding at surface sites, lattice vibrations at the surfaces/interfaces of most materials are at frequencies different than those in the bulk [15], a phenomenon observed in most solids. The chemical reactivity and electronic properties at surfaces and interfaces of materials are also different than those in the bulk [15]. It is, therefore, expected that the amount of energy required to break bonds at the LiOH/vacuum interface is not as large as in the bulk. In addition, in an environment where there is a moisture sink or in the case of a continuously pumped vacuum chamber, H₂O vapor is continuously removed and LiOH decomposes into Li₂O from the LiOH/vacuum interface (where it is thermally less stable) inward according to reaction (6) in an effort to maintain the equilibrium H₂O vapor pressure at the sample/vacuum interface. Since the equilibrium vapor pressure of H₂O over the LiOH/Li₂O

system is dependent exponentially on temperature [16], the thermal vacuum decomposition of LiOH is also a function of temperature. The inward vacuum thermal decomposition of LiOH into Li₂O releasing H₂O is qualitatively illustrated in the cartoon of fig. 3.

In a closed system containing both LiH and LiOH, the H₂O released from the decomposition of LiOH reacts with LiH to form hydrogen gas according to reaction (2). Such is the case of vacuum thermal decomposition of a corrosion layer previously grown on top of a LiH substrate. Here, at room temperature, the equilibrium H₂O vapor pressure near the Li₂O/LiH interface (according to the phase diagram in fig. 1) can be well below 10⁻⁴⁰ Pa while that near the Li₂O/LiOH interface is on the order of 10⁻¹³ Pa (see fig. 1). The huge H₂O concentration gradient across the Li₂O buffer layer in between the hydrophilic LiH substrate and LiOH, coupled with the defective nature of LiOH at surfaces/interfaces as discussed above, effectively lowers the energy barrier for LiOH decomposition here in comparison with bulk LiOH and turns the LiH substrate into an effective moisture pump [10, 13]. As a result, in the case of vacuum thermal decomposition of LiOH on top of a LiH substrate, the LiOH decomposition front starts at the LiH/Li₂O/LiOH interface. As a function of increasing time and temperature, the Li₂O layer in between LiH and LiOH gets thicker, causing the energy barrier for the LiOH decomposition at the LiOH/Li₂O/LiH interface to increase, and eventually LiOH at the LiOH/vacuum interface also starts to decompose into Li₂O for reasons described in the previous paragraph. Thereafter, the Li₂O fronts keep moving inward from all directions until all the LiOH is gone. This vacuum thermal decomposition process of LiOH previously grown on top of a LiH substrate is illustrated in the cartoon of fig. 4.

It will be shown in the kinetic measurement section of this chapter that the activation energy for the thermal decomposition of LiOH does not stay constant. It increases from the

lowest value of ~ 88 kJ/mol at the LiOH/Li₂O/LiH interface to an intermediate value of ~ 117 kJ/mol at the LiOH/vacuum interface and ultimately to a value above 134 kJ/mol for bulk LiOH. For dry/vacuum device applications involving temperatures not more than a few tens of degrees higher than room temperature, the LiOH decomposition practically never gets to the final stage presented in fig. 4. This will be discussed more in later sections.

In short, hydrogen outgassing from LiH occurs when LiH reacts with moisture to form a corrosion layer. In the absence of an external moisture source, hydrogen outgassing results from the decomposition of the LiOH corrosion layer in the presence of LiH.

GROWTH AND MORPHOLOGY OF THE CORROSION LAYER ON LITHIUM HYDRIDE

Fig. 5(a) shows an SEM image [17] of a polycrystalline LiD sample used in some of the experiments reported in this chapter. This sample was manually fractured into two smaller pieces in laboratory air with 30-40 % RH. The LiD sample was composed of grains with an average size on the order of hundreds of micrometers. A similar range of grain sizes is also observed for polycrystalline LiH samples mentioned in this chapter. Upon exposure to laboratory air, a corrosion layer with grain sizes in the range of tens of nanometers was seen to form on top of the polycrystalline LiD sample [fig. 5(b) and (c)]. An AFM image [18] of the surface of a polycrystalline LiH sample after laboratory air exposure, shown in fig. 6, also exhibits similar formation of a corrosion layer composed of nanometer scale grains. The top portion of fig. 6 shows a line scan across the surface. Various morphologies of LiOH films grown on polycrystalline LiH surfaces are shown in SEM images in fig. 7. Depending on the LiH substrate facets, LiOH corrosion layers may be composed of: columnar structures with average width on

the order of a few hundred nanometers (a), nanometer-scale grains (b), wave like structures (c), and some complex nanometer-scale structures (d). Fig. 7(a)-(d) were obtained by exposing a clean polycrystalline LiH surface to roughly 15 minutes of room air with $\sim 30\%$ RH at 296-300 K. Due to large lattice and volume mismatches among LiH, Li₂O, and LiOH [19], the formation of these nanometer-scale structures can be understood as a stress/strain relief measure for the growth of the corrosion layer.

To study the nature of the corrosion layer as a function of moisture exposure time, a razor blade was used to scrape the surface of a freshly cut polycrystalline LiD sample in laboratory air. This scraping action in $\sim 40\%$ RH produced a powder composed of LiD inner cores covered with lithium hydroxide outer layers as evidenced by x-ray diffraction (XRD) (see fig. 8). The diffraction peaks labeled 1, 2 and 3 correspond to LiD, LiOH and lithium hydroxide monohydrate (LiOH·H₂O) respectively. After about 2 hours of air exposure, some lithium hydroxide began to transform into LiOH·H₂O. The fact that the buffer layer of Li₂O in between LiH and LiOH was not detectable by XRD implies that it was very thin (perhaps less than a few nanometers at room temperature). The XRD results here are in agreement with the model for the growth of corrosion layers on LiH/LiD presented in the previous section.

The growth of the corrosion layer on LiH/LiD as a function of moisture exposure time was also reported to be parabolic in the initial stage when the corrosion layer is very thin (nanometer-scale thickness) and becomes linear in the later stage when the corrosion layer thickness reaches many micrometers [20]. Fig. 9 shows the time dependence of the hydrogen production probability (measured by the technique of modulated molecular beam mass spectrometry) and the Li₂O coverage (measured simultaneously by Auger electron spectroscopy) upon exposing a fresh LiH surface in an ultrahigh vacuum environment to a 1.3×10^{-5} Pa H₂O

molecular beam [20]. The hydrogen production probability was initially 0.11 and gradually reduced to 0.007 as the surface concentration of Li_2O reached the monolayer coverage. Fig. 10 shows the hydrogen production probability and the associated phase lag of the detected hydrogen with respect to the scattered H_2O molecules [20] as a function of H_2O exposure time. As the Li_2O film grew beyond a monolayer, the phase lag of hydrogen product increased from zero to 20 degrees and the reaction probability reduced further. This observation suggests that during the early stage of moisture exposure, diffusion of H_2O (probably in the form of OH^-) through the Li_2O layer to react with the LiH substrate is the rate limiting step in the growth of the corrosion layer. As the Li_2O layer reaches a certain characteristic thickness, the rate at which Li_2O is formed at the $\text{Li}_2\text{O}/\text{LiH}$ interface [according to reaction (2)] equals the rate at which Li_2O is converted to LiOH at the $\text{Li}_2\text{O}/\text{LiOH}$ interface [according to reaction (3)]. When this happens, a linear steady state growth stage begins and the Li_2O buffer layer retains, thereafter, a constant characteristic thickness [10]. In fig. 11, a plot of the hydroxide thickness vs. moisture exposure time is presented. The LiOH thickness was measured by exposing the $\{100\}$ surface of a LiD single crystal to laboratory air with 50% RH and examining its cross section using SEM [20]. It is seen from this plot that the corrosion growth rate is constant in the regime of micrometer thick hydroxide layer. This also implies that H_2O transport through the growing LiOH layer is much faster than the diffusion of H_2O through the Li_2O buffer layer. In this regime of thicker LiOH film growth, micro cracks generated in the film to release stress provide easy pathways for moisture to reach the Li_2O buffer layer. Experimental evidence of cracks in the thick LiOH structure has been reported [7]. SEM images of the cross section of a very thick LiOH film grown in air with 30-40% RH on the $\{100\}$ surface of a single crystal LiD are shown in Fig. 12(a) and (b). Columnar growth is clearly observed for the LiOH film grown on the $\{100\}$ plane

of LiD. Fig. 12 (c) shows the SEM image of the same film looking from the top down. Columnar structures with voids and open spaces are distinctly seen in this image. However, voids and cracks are rare in thinner hydroxide films (one micrometer thick or less) grown on LiH/LiD. Cracks are, however, observed to form even in thin corrosion layers during heat-treatment to convert hydroxide into lithium oxide due to the same stress/strain release mechanism discussed above[13-14, 21]. Images of Li₂O layers formed on LiH samples by decomposing the LiOH layers at 550 K in vacuum are presented in fig. 13. In general, the corrosion films under investigation were less than 1.5 μm thick and retained the majority of their integrity even after being converted to Li₂O. However, local spallation [the right portion of fig. 13(a) and (d)], blistering with spallation [fig. 13(b)], and blistering with cracks in the vicinity [fig. 13(c)] were seen. This is in stark contrast to thick (>> 1 μm) LiOH corrosion layers which tend to develop a large network of cracks to relieve stress during growth.

KINETIC MEASUREMENT AND PREDICTION OF HYDROGEN OUTGASSING

- **Experimental Method & Analysis:**

Hydrogen outgassing from the LiH/Li₂O/LiOH system was investigated mainly by the technique of TPR. A schematic diagram of the TPR experimental setup is shown in fig. 14. In a typical TPR experiment, the sample was attached to a sample holder by way of mechanical clamps and transferred, through a differentially pumped load lock, into an ultrahigh vacuum (UHV) sample chamber with a base pressure of 10⁻⁶ Pa. Within the sample chamber, the sample holder sat on a rotatable XYZ manipulator. The sample temperature was measured via a type K thermocouple inserted between the sample's front surface and one of the mounting clamps. Linear heating was achieved by passing current through a tungsten coil located 2 mm behind the

sample. The heating rate was computer-controlled. The sample chamber was connected by a 6 mm diameter orifice to a separately pumped detector chamber equipped with a Balzers quadrupole mass spectrometer which was in line of sight of the sample. The base pressure in the detector chamber was usually less than 10^{-7} Pa. During TPR experiments, the sample was positioned ~ 2 mm from the orifice facing the detector chamber. This arrangement guaranteed that only gases originating from the portion of the sample in line with the 6 mm orifice contributed to the gas flux detected by the quadrupole mass spectrometer.

Experiments were performed mainly on 1 mm thick pressed polycrystalline LiH (100 μm to 200 μm grain size) with heating rates in the range of 0.0005 K/s - 0.25 K/s. The TPR experiments reported here involved two types of LiH samples: fresh and baked. Here, the term fresh samples refers to LiH samples that have been polished with 1200 (P-4000) grit silicon carbide sand paper to remove hydroxide/oxide surface layers and then exposed to moisture levels of interest for pre-determined lengths of time prior to introduction into the TPR chamber. Polishing polycrystalline LiH samples with 1200 (P-4000) grit silicon carbide sand paper in a dry nitrogen purged glove box (water vapor partial pressure of 0.4-1.33 Pa) produced shiny LiH surfaces. Subsequent transport of the samples from the glove box to the TPR chamber in a vacuum container followed by 3 hours of exposure to 36 Pa of H_2O in the introduction chamber resulted in the formation of a roughly 93 nm thick LiOH corrosion layer as determined by the mass spectrometer employed in TPR experiments. In some cases, the polishing was performed in laboratory air with 30-40% RH and the samples were left in the same laboratory air for 21- 30 minutes prior to being loaded in the TPR chamber, resulting in a corrosion layer on the order of 1.2 μm thick. Baked samples were fresh samples with a 1.2 μm corrosion layer which had been heated to between 550 K and 580 K in a vacuum to convert all hydroxide into oxide (as verified

by monitoring the H₂O evolution with a mass spectrometer). After cooling under high vacuum, the baked samples were then re-exposed to 3 Pa of water vapor for 2.5 hours. This H₂O exposure resulted in the formation of a quantity of LiOH equivalent to a LiOH layer with a mean thickness of 0.28 μm. TPR was also performed on laboratory grade bulk LiOH powder with grain sizes in the range of many tens to many hundreds of micrometers obtained from Fisher Chemicals. Bulk LiOH powder samples for TPR experiments were prepared by wrapping about 45 mg of LiOH powder in square (1 cm on a side) platinum envelopes. The envelopes were constructed from 0.025 mm thick platinum foil. The side of each platinum envelope facing the mass spectrometer was perforated so that gases generated from the samples during heating could freely flow toward the mass spectrometer.

After the TPR spectra were obtained, the kinetics of the reactions was extracted by analyzing the TPR spectra of similarly prepared samples at different heating rates in accordance with the isoconversional method of thermal analysis as described below.

The rate equation for a solid-state reaction can be written as [22-25]:

$$\frac{d\alpha}{dt} = kf(\alpha) = \nu e^{-\frac{E}{RT}} f(\alpha) \quad (7)$$

where t is time, α is the reacted fraction (0 to 1), k is the rate constant, $f(\alpha)$ is an analytical function determined by the rate-limiting reaction mechanism, E is the activation energy for the rate controlling process, R is the gas molar constant, T is temperature in Kelvin, and ν is the pre-exponential factor describing the initial state of the sample (particle shape, molecular mass, density, stoichiometry, number of lattice imperfections, and so forth).

With a heating rate of $\beta = dT / dt$:

$$\frac{d\alpha}{dT} = \left[\frac{\nu}{\beta} f(\alpha) \right] e^{-\frac{E}{RT}} \quad (8)$$

Taking the natural logarithm on both sides of equation (8) yields

$$\ln\left(\frac{d\alpha}{dt}\right) = -\frac{E}{RT} + \ln\{\nu f(\alpha)\} \quad (9)$$

A plot of $\ln(d\alpha/dt)$ vs. T^{-1} at some α value for a set of β values has the slope $-E/R$ [26-27]. A

plot of E vs. α is thus obtained by repeating the above procedure at other chosen α values

between 0 and 1. This kinetic extraction procedure was first proposed by Friedman [26]. It is the

most general among all methods using derivatives but, like all derivative methods, suffers

inherent errors arising from noisy $d\alpha/dt$ values (most severely near the beginning and the end of the reaction).

Alternately, equation (7) can be rewritten as:

$$g(\alpha) = \int_0^\alpha \frac{d\alpha}{f(\alpha)} = \int_{T_0}^T \nu \exp\left(-\frac{E}{RT}\right) dt \quad (10)$$

Where T_0 denotes the temperature at which the TPR experiment starts. Usually, ν is not a

function of T and $d\alpha/dt = 0$ at $T \leq T_0$. Then, in the notation of $x \equiv E/RT$, equation (10) becomes:

$$\beta \frac{R}{\nu E} \int_0^\alpha \frac{d\alpha}{f(\alpha)} = \int_x^\infty x^{-2} \exp(-x) dx \quad (11)$$

The right hand side of equation (11) is also known as the temperature integral, $p(x)$, which has no

analytical solution in closed form but can be approximated. The Kissinger-Akahira-Sunose

(KAS) method adopts the approximation:

$$p(x) \cong \exp(-x)/x^2 \quad (20 < x < 50) \quad (12)$$

so that, numerically,

$$\ln\left(\frac{\beta}{T^2}\right) \cong -\frac{E}{R}\left(\frac{1}{T}\right) - \ln\left\{\left(\frac{E}{R\nu}\right) \int_0^\alpha \frac{d\alpha}{f(\alpha)}\right\} \quad (20 < E/RT < 50) \quad (13)$$

A plot of $\ln(\beta/T^2)$ vs. T^{-1} at some α value for a set of β' has the slope $-E/R$ [27-29].

The Ozawa-Flynn-Wall (OFW) method takes another approximation:

$$\log p(x) \cong -2.315 - 0.4567x \quad (20 < x < 60) \quad (14)$$

so that, numerically,

$$\ln(\beta) \cong -1.052 \frac{E}{R} \left(\frac{1}{T} \right) - 5.333 - \ln \left\{ \left(\frac{R}{\nu E} \right) \int_0^\alpha \frac{d\alpha}{f(\alpha)} \right\} \quad (20 < E/RT < 60) \quad (15)$$

A plot of $\ln(\beta)$ vs. T^{-1} at some α value for a set of β 's has the slope $-1.052E/R$ [27, 30-31].

Since the KAS and OFW methods are integral based techniques, they are usually better-behaved than the derivative based Friedman method, especially near the beginning and end of the experiments. In practice, due to a general problem of a poor signal-to-noise ratio near the beginning and the end of most chemical reactions, only data inside an α window of 0.1-0.9 are analyzed for kinetic extraction even with the KAS and OFW methods, which are used for all kinetics extractions for the rest of this chapter. It is noted that these variations of the isoconversional technique of analyzing TPR spectra do not assume any particular rate limiting model.

- **Results & Discussion:**

The Gibbs free energies associated with the reactions of LiH with H₂O as described in reactions (2) and (3) at room temperature are roughly -47 kcal/mol and -22 kcal/mol, respectively [5]. Thermodynamically, the formation of an oxide/hydroxide corrosion layer on LiH is very favorable. In an environment with a high partial pressure of water vapor, the growth of the oxide/hydroxide corrosion layer is relatively fast. For example, at room temperature and 50% RH, the growth of the hydroxide corrosion layer in the steady growth stage is on the order of 0.4nm/s (see fig. 11). In most industrial or device applications, LiH is placed in either an initially dry or a vacuum environment with other materials that may release moisture slowly over many months, years, or even decades. In such instances, the rate of hydrogen outgassing from

the reaction of LiH with H₂O can be reasonably approximated by the rate at which H₂O is released from the moisture containing materials [32] and will not be discussed any further. For remainder of this chapter, the focus will instead be on measuring the kinetics of hydrogen outgassing as a result of the thermal decomposition of LiOH (previously grown on LiH) in a dry or vacuum environment without the presence of any moisture containing material.

Fig. 15 (a), (b) and (c) show H₂ (darker solid lines) and H₂O (lighter solid lines) TPR spectra, at a heating rate of 0.025 K/s, of fresh LiH samples with 93 nm, 1.2 μm and 36 μm thick LiOH surface corrosion layers, respectively. Fig. 15(d) shows H₂O TPR spectrum obtained at the same heating rate from bulk LiOH powder for comparison. The H₂ emission from the fresh LiH sample with a 93 nm LiOH corrosion layer occurs over a broad temperature range from 300 K to 530 K and exhibits 2 peaks: one around 420 K and another around 480 K. H₂ evolution from the fresh LiH sample with a 1.2 μm thick LiOH corrosion layer covers a temperature range from 300 K to 550 K and is heavily biased toward higher temperatures with a peak around 510 K. The H₂ TPR spectrum for the fresh LiH sample with a 36 μm thick LiOH corrosion layer exhibits a peak at an even higher temperature (~ 600 K). From the data, it appears that the energy barrier for H₂ outgassing from LiH increases with LiOH film thickness. The H₂O signals recorded in the TPR spectra originated from the vacuum thermal decomposition of LiOH according to reaction (6). The H₂O signal from the fresh LiH sample with a 93 nm thick LiOH corrosion layer is very weak, but non-zero, below 475 K with a clear peak around 480 K. The fresh LiH sample with a 1.2 μm thick LiOH corrosion layer shows a much stronger H₂O signal at around 510 K. For the fresh LiH sample with a 36 μm thick LiOH corrosion layer, the peak of the H₂O signal shifts to 600 K while that from bulk LiOH powder exhibits a peak at around 610 K. Qualitatively, it seems like the energy barrier for the vacuum thermal decomposition of LiOH is significantly

lower for thin LiOH films grown on LiH and increases with increasing thickness of the corrosion layer, eventually reaching the value of bulk LiOH powder decomposition for thick LiOH films. In the temperature range below 475 K, the measured intensity of H₂ is much higher than that of H₂O. The fact that the H₂O signal is non-zero in the temperature range below 475 K confirms that the thermal decomposition of LiOH according to reaction (6) is taking place in this temperature range for LiOH grown on the surface of LiH. The presence of the much stronger H₂ intensity in this temperature range suggests that most H₂O molecules generated from the decomposition of LiOH diffuse quickly through the Li₂O buffer layer in between LiOH and LiH to react with LiH according to reaction (2). The sequel of reactions responsible for the H₂O and H₂ outgassing in the lower temperature range where the ratio of H₂ signal to H₂O signal is very high are:



Why is the ratio of intensities of H₂ to H₂O so high below 475K? A plausible explanation is that at lower temperature, LiOH near the LiOH/Li₂O/LiH interface starts to decompose first according to reaction (16). Due to its close vicinity to the LiH substrate, which acts as a moisture sink, most H₂O molecules created from reaction (16) quickly diffuse through the thin Li₂O buffer layer to react with LiH to form H₂ gas according to reaction (17). As the temperature increases, the Li₂O buffer layer between the LiH substrate and LiOH gets thicker while LiOH from the vacuum/LiOH interface also starts to decompose inward toward the bulk as illustrated in figs. 3 and 4. The rate of LiOH inward decomposition increases exponentially with temperature, as can be seen in equation (7). Beyond 475 K, the rate of vacuum thermal decomposition of LiOH becomes very high and the Li₂O buffer layer between LiH and LiOH is sufficiently thick that a

good fraction of H₂O generated by reaction (16) can escape from the sample and is detected by the mass spectrometer. The almost perfect alignment of the hydrogen peaks with the water peaks above 475 K, as seen in fig. 15(a), (b) and (c), implies that the rate limiting step in the process of hydrogen outgassing from LiH is the actual decomposition of LiOH, not the diffusion of H₂O [33] through the Li₂O buffer layer. In a closed system containing LiH and LiOH, all H₂O generated from LiOH decomposition rapidly reacts with LiH to form H₂ [6]. Thus, in the absence of any external H₂O source, LiOH is involved in all aspects of hydrogen outgassing from the LiH/Li₂O/LiOH system.

From the sequential reactions (16) and (17), it can be seen that two LiOH decomposition events generate one intermediate H₂O molecule which, in turn, produces two H₂ molecules. Overall, there is one mole of H₂ formed for the decomposition of one mole of LiOH. Therefore, in vacuum device applications involving both LiH and LiOH, the total equivalent hydrogen outgassing flux ($\Gamma_{\text{equiv. hydrogen}}$, in units of molecules.m⁻².s⁻¹) resulting from all LiOH decomposition events can be approximated by doubling the H₂O TPR flux ($\Gamma_{\text{H}_2\text{O}}$) and adding the results to the H₂ TPR flux (Γ_{H_2}):

$$\Gamma_{\text{equiv. hydrogen}} = 2\Gamma_{\text{H}_2\text{O}} + \Gamma_{\text{H}_2} \quad (18)$$

Fig. 16 shows TPR spectra, at different heating rates, of the total equivalent H₂ release rates in units of molecules.m⁻².s⁻¹ from (a) fresh LiH with a 93 nm thick LiOH corrosion layer, (b) fresh LiH with a 1.2 μm thick corrosion layer, (c) baked LiH (with a subsequent exposure to 3 Pa of H₂O for 2.5 hours), and (d) LiOH powder. In all cases, the maximum outgassing peak shifted to higher temperature as the heating rate was increased. The outgassing peak shifts presented in fig. 16 are on the order of many tens of degrees in going from the slowest heating rate to the fastest heating rate in each set of data. The peak shifting to a higher temperature with

increasing heating rate is consistent with a thermal process with a positive activation energy barrier.

Plots of E vs. α for fresh LiH samples, baked LiH samples and bulk LiOH powder are presented in figs. 17 (a) and (b). In fig. 17, the dashed and solid lines are activation energy barriers derived from the OFW and KAS methods, respectively. The activation energy barrier for the outgassing process from fresh LiH samples is seen, in fig. 17(a), to increase with the reacted-fraction, α , and the LiOH film thickness. This is easily seen if the activation energy barrier for outgassing is plotted against the equivalent LiOH decomposition thickness for fresh LiH samples [fig. 18], where the LiOH decomposition thickness, x_{LiOH} , is estimated from:

$$x_{LiOH} = \frac{m_{LiOH}}{\rho_{LiOH}} \int \frac{\Gamma_{equiv. \text{ hydrogen}}}{\beta} dT \quad (19)$$

In equation (19), m_{LiOH} (3.99×10^{-26} kg.molecule⁻¹) and ρ_{LiOH} (1460 kg.m⁻³) are the mass of a LiOH molecule and the density of bulk LiOH, respectively. During moisture exposure, most of the LiOH formed early in the process is interface/surface LiOH. However, there is a limit to the number of sites available to form interface/surface LiOH. Once these sites are used up, the remaining LiOH creation is almost exclusively bulk. As a result, one expects an inverse relationship between the activation energy barrier for hydrogen outgassing in the LiH/LiOH system and the LiOH corrosion layer thickness. From fig. 18, it is seen that the activation energy barrier for the decomposition of LiOH starts out at a low value of ~ 88 kJ/mol for interfacial LiOH (LiOH states within a ~ 60 nm distance from the LiH/Li₂O interface). This activation energy barrier increases quickly to ~ 117 kJ/mol for an LiOH corrosion layer thickness of about 100 nm and approaches the value for bulk LiOH decomposition (> 134 kJ/mol) when the corrosion layer surpasses a thickness of about 1 μ m. The activation energy barrier for hydrogen outgassing from baked LiH samples [fig. 17(b)] is lower, and has a different shape than that of

fresh LiH samples with a mean LiOH layer thickness of 1.22 μm [fig. 17(a)], from which the baked LiH samples were made. The cartoon in fig. 19 illustrates the re-hydroxylation process following vacuum baking and subsequent low moisture exposure through the cross-section of a hypothetical fresh LiH sample. Vacuum baking of the LiH/LiOH system at high temperature converts LiOH into Li_2O . During baking, local spallations and cracks are formed within the Li_2O to relieve stress. Upon subsequent low H_2O exposure for a short duration, only a small amount of Li_2O (primarily near the surface and in cracks) is converted back to, mostly, surface LiOH. This is because Li_2O surface states (near the vacuum/surface and in cracks) are readily accessible to H_2O molecules and are converted to LiOH surface states first. Li_2O near the $\text{Li}_2\text{O}/\text{LiH}$ interface is less accessible to H_2O molecules, except near cracks. Bulk Li_2O and interfacial Li_2O near the $\text{Li}_2\text{O}/\text{LiH}$ interface are converted to LiOH last and only in longer moisture exposures since it takes time for H_2O molecules to diffuse inward to reach these locations. As explained earlier, surface LiOH is thermally more stable than interface LiOH but less stable than bulk LiOH. In addition, the ratio of surface LiOH to interface and bulk LiOH is much higher in systems baked and subsequently exposed to low H_2O pressure for a short duration. The activation energy barrier for the decomposition of LiOH formed on baked samples is, therefore, expected to cover the range of values in between that of interface LiOH (~ 60 nm of LiOH closest to the LiH/ Li_2O interface on fresh LiH samples) and that of bulk LiOH (many micrometers thick LiOH layer on fresh LiH samples). From the plots of E vs. α in fig. 17, surface LiOH states are deduced to have thermal decomposition activation energies higher than 88 kJ/mol (interface LiOH) but lower than 134 kJ/mol (bulk LiOH). LiOH states at or near the LiOH/vacuum interface have higher activation energy barriers than and contribute less than interfacial LiOH states to outgassing at lower temperatures. Bulk LiOH, with an activation energy barrier of decomposition

greater than 134 kJ/mol, is thermally stable, even at 350 K in a good vacuum, and practically causes no outgassing concern in device applications. Since hydrogen outgassing from the LiH/LiOH system, in the absence of an external moisture source and at lower temperatures, is attributed mostly to interface LiOH and, to a lesser degree, surface LiOH, it is dependent more on the sample's geometrical surface area than on the LiOH corrosion thickness.

OUTGASSING KINETIC PREDICTION

- **Isoconversional Kinetic Prediction Method:**

Using the integral form of the rate equation [equation (10)] for isothermal conditions gives:

$$g(\alpha) = \left[\nu e^{-\frac{E}{RT}} \right] \int dt = \left[\nu e^{-\frac{E}{RT}} \right] t \quad (20)$$

For non-isothermal conditions with a constant heating rate, β , [34]:

$$g(\alpha) = \frac{\nu}{\beta} \int_0^T e^{-\frac{E}{RT}} dT \approx \frac{\nu}{\beta} \frac{RT^2}{E} e^{-\frac{E}{RT}} \quad (21)$$

Depending on the accuracy needed for the applications of interest, more elaborate (but at the cost of simplicity) approximations to the analytical solution to the $g(\alpha)$ expression for non-isothermal conditions have been documented [35].

The time, t_α , at which a given conversion, α , is reached at an arbitrary temperature T_o can be approximated from non-isothermal experiments for many processes by equating the $g(\alpha)$ forms above for the isothermal and non-isothermal conditions [36-37]:

$$t_\alpha = \left[\beta e^{-\frac{E_\alpha}{RT_o}} \right]^{-1} \frac{RT_\alpha^2}{E_\alpha} e^{-\frac{E_\alpha}{RT_\alpha}} \quad (22)$$

Here, T_α is the temperature corresponding to a given conversion α at the heating rate of β . E_α is the experimentally determined value of the overall activation energy barrier at that level of conversion. Thus, using values of E_α vs. α obtained from the KAS or OFW methods, a TPR spectrum with a heating rate of β can, with equation (22), be used to predict α as a function of time for a given temperature, T_0 . To scale up the results from the above kinetic prediction (which is derived from experiments on small samples) for comparison with actual isothermal outgassing experiments involving large samples, the geometrical surface area of the LiH sample has to be taken into account according to the simple formula:

$$\text{Total outgassing} = \text{outgassing per unit area} \times \text{geometrical area of the LiH sample} \quad (23)$$

Using the methodology presented here, time dependent kinetic predictions for hydrogen release from the LiH/LiOH system can be made at any temperature and as a function of sample pre-treatment. The isoconversional method of kinetic measurement and prediction presented in this chapter has advantages as well as disadvantages. Its primary advantage is that it is a model-independent technique which has all the known/unknown reactions embedded in data from a series of dynamic thermal experiments on identical samples at different heating rates. The main disadvantage of the isoconversional method is that it requires collection of data from a set of very similarly prepared and treated samples at widely different heating rates.

- **Kinetic prediction**

In order to test the validity and accuracy of kinetic measurements and predictions based on the isoconversional analysis of TPR outgassing spectra, a set of long-term (i.e. > 180 days) isothermal outgassing experiments were undertaken. The isothermal outgassing experiments involved stored LiH and annealed LiH. Stored LiH was maintained in an environment with ≤ 10

ppm of H₂O, over an extended period of time, until insertion into previously baked and thoroughly outgassed UHV stainless steel containers, each equipped with a Baratron capacitance manometer gauge for measuring pressure and two valves to allow pump-down (by a turbo molecular pump) and gas sampling. Annealed LiH was stored LiH which had been annealed in a vacuum of $< 1.3 \times 10^{-4}$ Pa at 503 K for 40 hours, cooled down and then re-exposed to 30 ppm of H₂O for 2-3 hours. Diffuse Reflectance Infrared Fourier Transform spectroscopy (DRIFT) indicated that the LiOH surface thickness was on the order of 0.26 μm for both stored LiH and annealed LiH. Similar to the case of fresh LiH and baked LiH described earlier, a significant reduction in the LiOH content is expected for annealed LiH in comparison with stored LiH. However, DRIFT measurements of LiOH thicknesses for stored LiH and annealed LiH were on the same order of magnitude. It is likely that DRIFT measurement of LiOH thickness on stored LiH and annealed LiH is not as sensitive as the mass spectrometer based measurement employed for fresh LiH and baked LiH. After pump down, the containers were placed within ovens set at different temperatures. Empty control vessels served to establish a background outgassing level. At the end of the isothermal experiments, the gas content in each container was analyzed and found to be mostly H₂ (~99% H₂ and ~ 1% trace amounts of N₂ + O₂ + Ar).

A comparison between experimental isothermal hydrogen outgassing from stored LiH, with a total geometrical surface area of 0.0190 m², and an outgassing prediction based on the model-free kinetic analysis for fresh LiH, with a similar surface area, at 343 K is presented in Fig. 20(a). Figs. 20(b), (c) and (d) show comparisons between experimental isothermal hydrogen outgassing from annealed LiH, with a total geometrical surface area of 0.0205 m², and outgassing predictions based on the model-free kinetic analysis for baked LiH at 348.7 K, 330.1 K and 315.5 K, respectively. The heavy lines indicate experimental isothermal hydrogen

outgassing data while the lighter bands are predicted from the isoconversional kinetic analysis of TPR spectra. Despite scatter in the experimental isothermal outgassing curves, experimental and predicted curves are in good agreement. Given the likely differences in preparation conditions and variations in LiH sample treatment between the TPR and isothermal experiments, it is remarkable that the isothermal data falls within the kinetic prediction bounds and, more importantly, that the curve shapes are well represented, adding credence to the kinetic prediction method presented here.

In fig. 21, plots of predicted α vs. time are presented for the vacuum thermal conversion of LiOH into Li₂O for a fresh LiH sample with a 93 nm corrosion layer at 300 K (a), for a baked LiH sample at 300 K (b), for bulk LiOH powder at 300 K (c) and for bulk LiOH powder at 343 K (d). The shaded bands around the prediction lines represent a 35 % associated error in the accuracy of the prediction models. From fig. 21, it is observed that bulk LiOH powder, which is composed of LiOH grains with sizes ranging from tens to hundreds of micrometers, is thermally very stable against vacuum decomposition into Li₂O and H₂O, even at 343K. For comparison, about 12-24 % of the LiOH in the baked LiH sample, which is composed mostly of surface LiOH, decomposed at 300K over many decades. Since the equivalent LiOH film thickness in the baked LiH sample is 0.28 μm , it is estimated that about 34-68 nm surface Li₂O would be formed at the sample/vacuum interface in one hundred years. In contrast, for the fresh LiH sample, 45-95% of the LiOH in the 93 nm corrosion layer, which is composed mostly of interfacial LiOH and some surface LiOH, decomposes in about twenty years at 300K.

OUTGASSING MITIGATION

As mentioned above, high temperature baking converts LiOH into Li₂O. Limited re-exposure of baked samples to moisture for a short duration of time forms surface LiOH near the sample/vacuum interface and around cracks (small amount of interface LiOH may also be formed if some of the cracks reach close to the LiH/Li₂O interface). Mitigating unwanted hydrogen outgassing from LiH, therefore, involves vacuum baking of LiH before device assembly and a few common-sense practices. If device applications require high temperature operation (well in excess of 343K), a thorough conversion of all LiOH into Li₂O is recommended. In this case, since the equilibrium vapor pressure of H₂O over the LiOH/Li₂O system at 500K is higher than 13 Pa [5], vacuum baking at 535K for a couple of days in a low vacuum environment is sufficient (fig. 22). However, since bulk LiOH is thermally stable in a good vacuum even at 343K [fig. 21(d)] and surface LiOH is unavoidable even with baking followed by low moisture exposure, it is practically sufficient to get rid of the least thermally stable interfacial LiOH. This can be achieved by baking LiH at 480 K in a high vacuum for a few hours (see fig. 23) if the operational temperature does not exceed 343 K. The advantage of vacuum baking LiH at a lower temperature for a shorter time is the reduction in crack formation, and thus the total amount of less stable interface and surface LiOH that might form after limited moisture re-exposure. After vacuum baking, assembly of LiH parts into devices should be performed in a dry room to minimize re-hydroxylation. Care should also be taken in the design of devices so as to minimize the amount of material that can release moisture over time in the same enclosure with LiH to avoid the direct reaction of LiH with H₂O to form hydrogen.

SUMMARY

LiH readily reacts with moisture to form a corrosion layer, releasing hydrogen gas. This corrosion layer is composed of a thin Li_2O buffer layer at the LiH substrate interface, followed by a layer of LiOH, which is then followed by another layer of $\text{LiOH}\cdot\text{H}_2\text{O}$ on top of the LiOH layer if the environment has a humidity level higher than 15% RH. The growth rate of this corrosion layer initially follows a parabolic behavior then becomes linear in later stage. This growth rate remains constant in the steady state when the corrosion layer thickness is in the micrometer range. Kinetic measurements show that the activation energy for the vacuum thermal decomposition of LiOH starts out at a low value of ~ 88 kJ/mol for interfacial LiOH (LiOH within a 60 nm distance from the LiH/ Li_2O interface). This activation energy barrier increases to an intermediate value of ~ 117 kJ/mol for surface LiOH (LiOH within a 34-68 nm distance from the LiOH/vacuum interface) and ultimately to a value above 134 kJ/mol for bulk LiOH. In a dry/vacuum environment, LiOH in the corrosion layer near the LiH/ Li_2O interface and near the LiOH/vacuum interface slowly decompose over many years and decades, respectively, even at room temperature into lithium oxide, releasing water vapor which then reacts with the lithium hydride substrate to form hydrogen gas. The outgassing associated with the vacuum thermal decomposition of LiOH into Li_2O is dependent on the LiOH corrosion layer thickness and baking treatments, and is directly proportional to the total LiH geometrical surface area. This hydrogen outgassing can potentially cause unwanted metal hydriding and/or compatibility issues elsewhere in the devices. In the course of this chapter, measurement and prediction of hydrogen outgassing using TPR and isoconversional analysis have been demonstrated. Practical techniques to mitigate the hydrogen outgassing problem based on various vacuum baking schemes were also discussed.

ACKNOWLEDGEMENT

This work was performed under the auspices of the U.S. Department of Energy, by the University of California, Lawrence Livermore National Laboratory under contract No. W-7405-ENG-48.

REFERENCES

1. Tyutyunnik V. I. , Phys. Stat. Sol. (b) 1992, **172**, 539-543.
2. Goertz St., Bradtke Ch., Dutz H., Gehring R., Meyer W., Plückthun M., Reicherz G., Runkel K., Thomas A., Nucl. Instr. and Meth. In Phys. Res. A 1995, **356**, 20-28.
3. Mueller W. M., Blackledge J. P., Libowitz G. G., *Metal Hydrides*, Academic Press, New York, 1968.
4. Welch F. H., Nucl. Eng. Des. **26** (1974) 444-460.
5. HSC Chemistry software, Outokumpu Research Oy, Finland.
6. Myers S. M., J. of Appl. Phys. 1974, **45**, 4320-4329.
7. Dinh L. N., Cecala C. M., Leckey J. H., Balooch M., J. Nucl. Mater. 2001, **295**, 193-204.
8. Dinh L. N., McLean W. II, Schildbach M. A., LeMay J. D., Siekhaus W. J., Balooch M., J. Nucl. Mater. 2003, **317**, 175-188.
9. Leckey J. H., Nulf L. E., Kirkpatrick J. R., Langmuir 1996, **12**, 6361-6367.
10. Phillips J., Tanski J., Int. Mater. Rev. 2005, **50**, 265-286.
11. Machin W. D., Tompkins F. C., Trans. Faraday Soc. 1966, **62**, 2205-2218.
12. McLaughlin J. F., Cristy S. S., Composition of Corrosion Films on Lithium Hydride Surfaces After Exposure to air, Oak Ridge Y-12 Plant, 1974, document Y-1929.

13. Dinh L. N., Grant D. M., Schildbach M. A., Smith R. a., Siekhaus W. J., Balazs B., Leckey J. H., Kirkpatrick J. R., McLean W. II, *J. Nucl. Mater.* 2005, **347**, 31-43.
14. McIntyre J. M., Smith H. M., American Chemical Society Paper Abstract for the S.E. and S.W. Regional Meeting, December 2nd – 4th 1970, 174.
15. Lüth H., *Solid Surfaces, Interfaces and Thin Films*, Springer, Berlin, 2001.
16. Takeshita H., Watanabe H., *J. Nucl. Mater.* 1993, **207**, 92-97.
17. All SEM images were obtained with a Hitachi field emission scanning electron microscope (model S4500) in the secondary electron mode.
18. AFM images were obtained with a Digital Nanoscope IV in tapping mode in ambient air.
19. LiH has a cubic structure with lattice parameter of $a = 4.0684 \text{ \AA}$ and a unit cell volume of 67.3 \AA^3 ; Li₂O has a cubic structure with lattice parameter of $a = 4.611 \text{ \AA}$ and a unit cell volume of 98.1 \AA^3 ; LiOH has a tetragonal structure with lattice parameters of $a = 3.553 \text{ \AA}$ and $c = 4.348 \text{ \AA}$ and a unit cell volume of 54.9 \AA^3 .
20. Balooch M., Dinh L. N., Calef D. F., *J. Nucl. Mater.* 2002, **303**, 200-209.
21. Holcombe C. E., Powell G. L., *J. Nucl. Mater.* 1973, **47**, 121-124.
22. Bamford C. H., Tipper C. H. F., *Comprehensive Chemical Kinetics: Reaction in the Solid State*, Elsevier, Amsterdam, 1980, Vol. 22, p. 41-114.
23. Heide K., Holand W., Golker H., Seyfarth K., Muller B., Sauer R., *Thermochim. Acta* **1975**, **13**, 365-378.
24. Gadalla A. M., *Thermochim. Acta* 1985, **95**, 179-200.
25. Galwey A. K., Brown M. E., *Thermal Decomposition of Ionic Solids*, Elsevier, New York, 1999.
26. Friedman H. L., *J. Polym. Sci. Part C*, 1964, **6**, 183-195.

27. Li C-R., Tang T. B., J. Mater. Sci. 1999; **34**, 3467-3470.
28. Kissinger H. E., Anal. Chemistry 1957, **29**, 1702-1706.
29. Akahira T., Sunose T., Trans. 1969 Joint Convention of Four Electrical Institutes, paper No. 246; Res. Report Chiba Inst. Technol. 1971, **16**, 22.
30. Flynn J. H., Wall L. A., J. Polym. Sci. Part B 1966, **4**, 323-328.
31. Ozawa T., Thermochemica Acta 1992, **203**, 159-165.
32. L. N. Dinh, Private Communication.
33. Currently, there is no experimental evidence of whether H₂O, generated from the LiOH thermal decomposition at the LiOH/Li₂O interface, diffuses through the Li₂O buffer layer as H₂O or as OH⁻. It is, however, more likely that OH⁻ is the actual diffusing species. A possible mechanism for H₂O to diffuse through the Li₂O buffer layer to react with LiH as OH⁻ has been proposed in ref. 13.
34. Van Heek K. H., Jüntgen H., Berichte Der Deutschen Bunsengesellschaft Für Physikalische Chemie 1968, **72**, 1223-1251.
35. Senum G. I., Yang R. T., J. Thermal. Anal. 1977, **11**, 445-447.
36. Vyazovkin S., Wight C. A., Annu. Rev. Phys. Chem. 1997, **48**, 125-149.
37. S. V. Vyazovkin, A. I. Lesnikovich, Russ. J. Phys. Chem. 1988, **62**, 1535-1537.

FIGURE CAPTIONS

Fig. 1: The phase stability diagram for lithium, hydrogen and oxygen at 298 K.

Fig. 2: A cartoon depicting the cross-sections of LiH samples that have been exposed to different moisture environments at 298K.

Fig. 3: The inward vacuum thermal decomposition of LiOH into Li₂O.

Fig. 4: A cartoon depicting the cross-sections of a LiH sample with a corrosion layer on top during vacuum thermal heating.

Fig. 5: (a) SEM image of a freshly cut polycrystalline LiD sample with grain sizes on the order of hundreds of micrometers; (b) A layer of nanostructures with grain sizes on the order of tens of nanometers was seen to form on top of the polycrystalline LiD sample after air exposure; (c) An area of (b) at a higher resolution.

Fig. 6: An AFM image of the surface roughness measured on a pressed polycrystalline LiH. The top portion of this figure shows a line scan across the surface.

Fig. 7: SEM images of LiOH corrosion layer grown on different facets of pressed polycrystalline LiH after 15 minutes of air exposure at 30% RH (a through d). Larger nanometer-scale grains observed by SEM on some facets of pressed polycrystalline LiH after exposure to room air for 40 minutes (e and f).

Fig. 8: XRD spectra of powder scraped off a pressed polycrystalline LiD surface in air with ~40% RH as a function of time.

Fig. 9: The time dependence of the reaction probability of H₂O with LiH through hydrogen production along with oxygen containing species coverage measured simultaneously by AES.

Fig. 10: The H₂O reaction probability and phase lag of desorbed hydrogen with respect to scattered water molecules for the H₂O/LiH reaction.

Fig. 11: Hydroxide thickness, X, as a function of moisture exposure time on LiD.

Fig. 12: Cross-section SEM images of a LiOH film grown in air with 30-40% RH [(a) and (b)] and SEM image of the same film looking from the top down (c).

Fig. 13: Occasional spallations, blisters and cracks were observed in the morphology of a less than 1.5 μm thick LiOH corrosion layer grown on polycrystalline LiH after heating to 550 K in vacuum.

Fig. 14: A schematic diagram of the TPR experimental setup.

Fig. 15: H_2 (darker solid lines) and H_2O (lighter solid lines) TPR spectra, at a heating rate of 0.025 K/s, for fresh LiH samples with 93 nm (a), 1.2 μm (b), 36 μm (c) thick LiOH surface corrosion layers and for bulk LiOH powder (d).

Fig. 16: TPR spectra, at different heating rates, of the total equivalent H_2 release rates in units of $\text{molecules}\cdot\text{m}^{-2}\cdot\text{s}^{-1}$ from (a) fresh LiH sample with a 93 nm thick LiOH corrosion layer, (b) fresh LiH sample with a 1.2 μm thick corrosion layer, (c) baked LiH sample, and (d) LiOH powder.

Fig. 17: Plots of E vs. α for bulk LiOH powder and fresh LiH samples (a) and bulk LiOH powder and baked LiH samples (b) according to the OFW (dashed lines) and KAS (solid lines) methods.

Fig. 18: Activation energy barrier for outgassing vs. the equivalent LiOH decomposition thickness for fresh LiH samples.

Fig. 19: A cartoon representing the re-hydroxylation process following vacuum baking and subsequent low moisture exposure at the cross-section of a hypothetical fresh LiH sample.

Fig. 20: Comparison between experimental isothermal hydrogen outgassing and isoconversional kinetic prediction for stored and fresh LiH samples at 343 K (a) and annealed and baked LiH samples at 348.7 K (b), 330.1 K (c) and 315.5 K (d).

Fig. 21: Predictions of α vs. time for the vacuum thermal conversion of LiOH into Li_2O at 300 K for the fresh LiH sample with a 93 nm corrosion layer (a), for the baked LiH sample (b) and for bulk LiOH powder (c).

Fig. 22: Predicted α vs. time for vacuum thermal conversion of bulk LiOH (near the LiH/Li₂O interface) into Li₂O at 535 K.

Fig. 23: Predicted α vs. time for vacuum thermal conversion of interfacial LiOH (near the LiH/Li₂O interface) into Li₂O at 480 K.

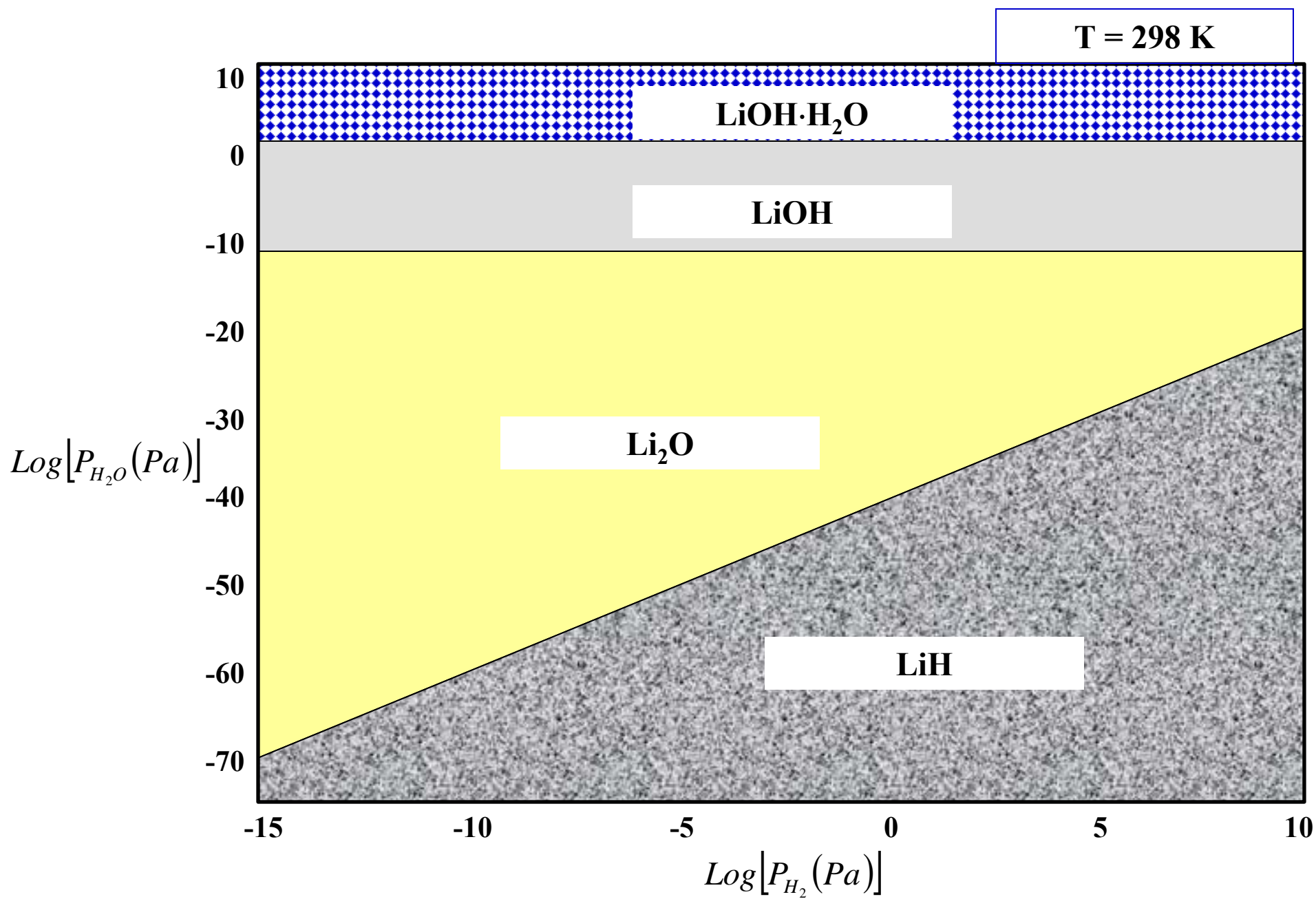

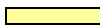

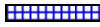
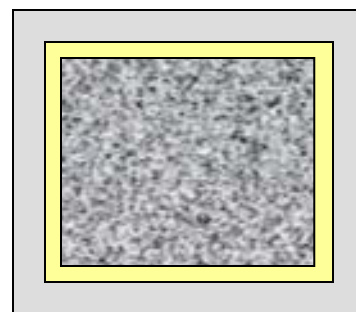


Fig. 1

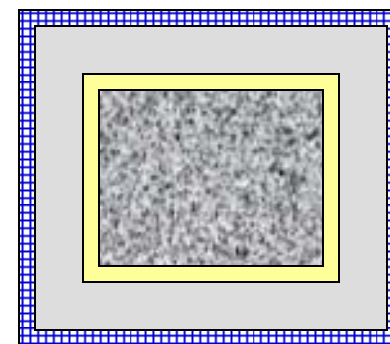
-  LiH
-  Li₂O
-  LiOH
-  LiOH·H₂O



298 K, H₂O partial pressure is less than 10⁻¹¹ Pa

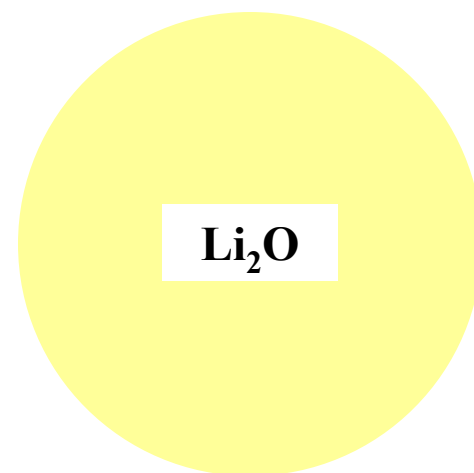
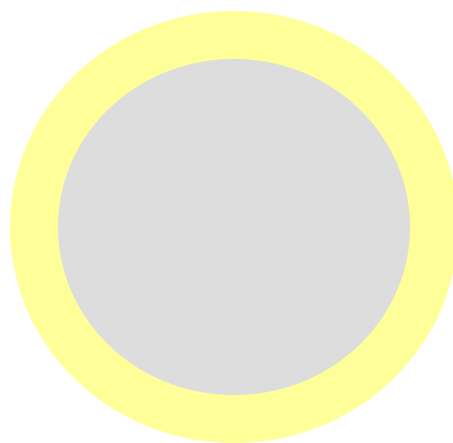
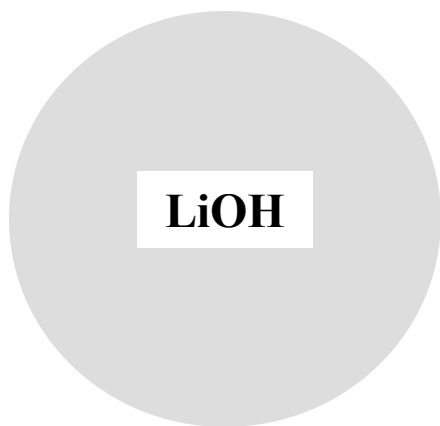


298 K, H₂O partial pressure is greater than 10⁻¹⁰ Pa but less than 10² Pa



298 K, H₂O partial pressure is greater than 10³ Pa

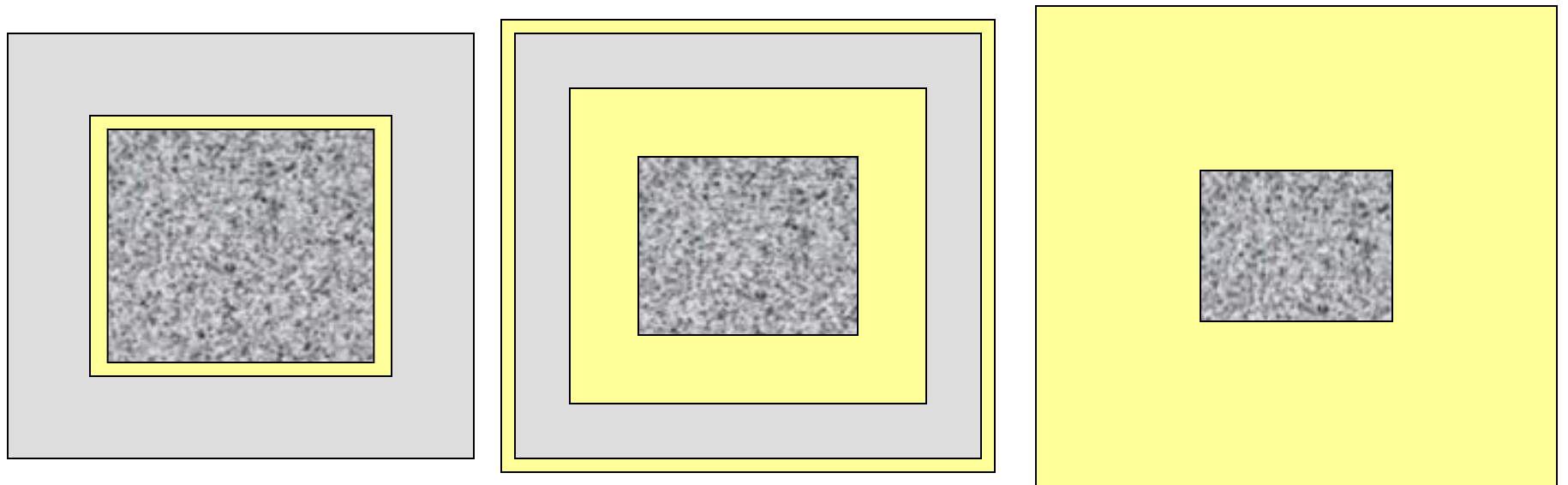
Fig. 2



Increasing time and temperature



Fig. 3

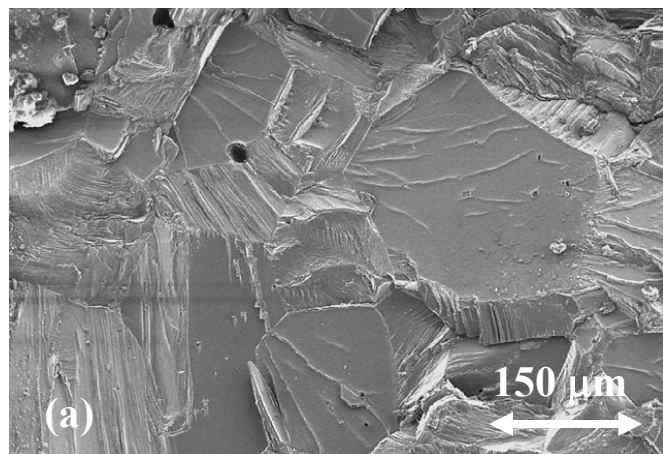


- LiOH
- Li₂O
- LiH

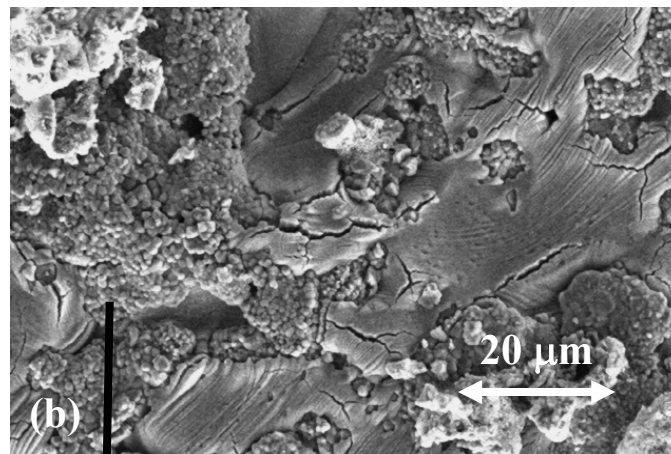
Increasing time and temperature



Fig. 4



Freshly prepared polycrystalline LiD



Upon air exposure

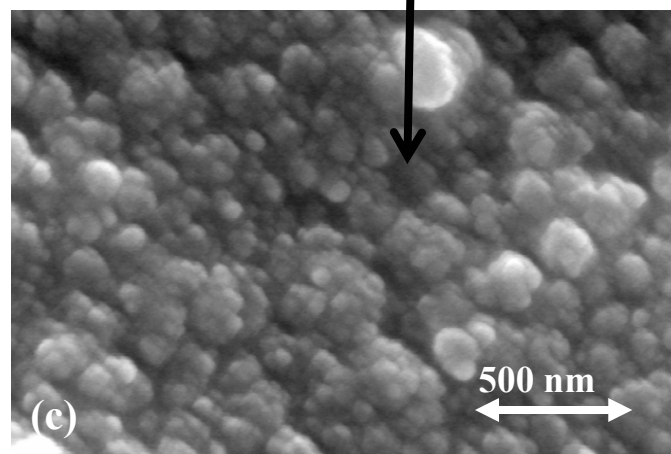


Fig. 5

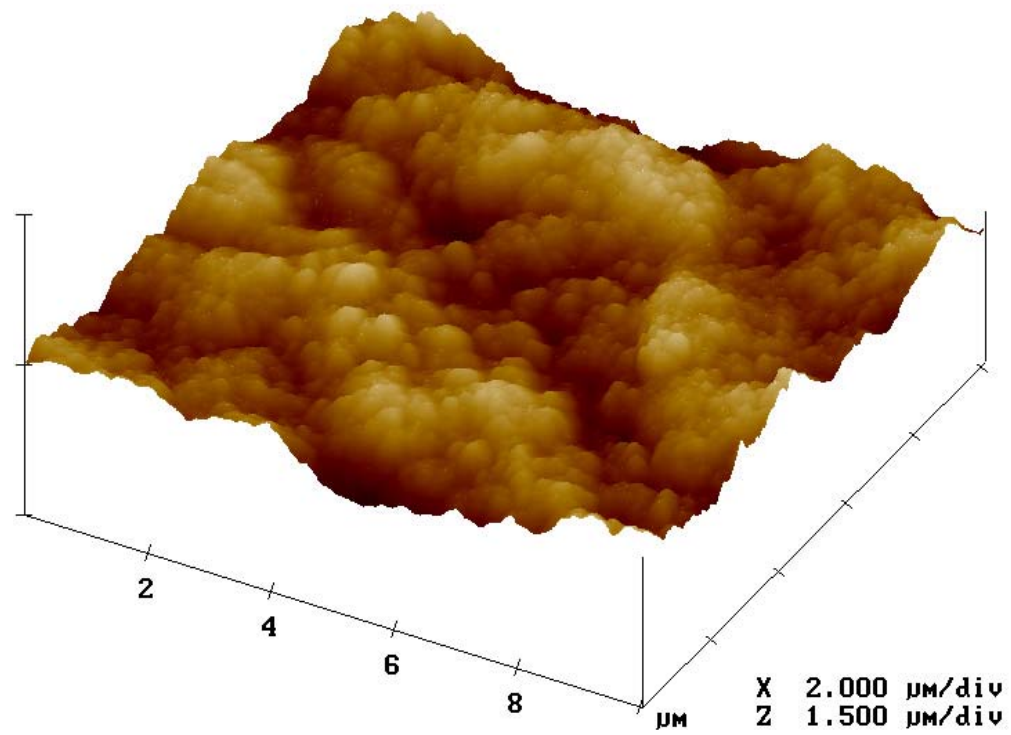
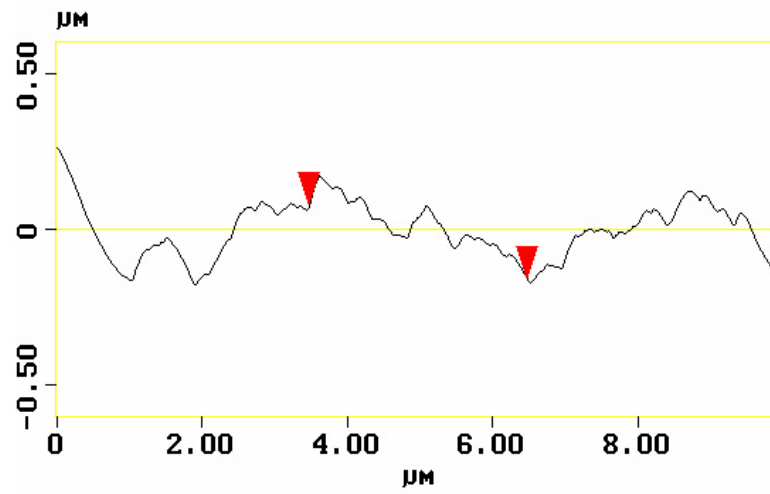


Fig. 6

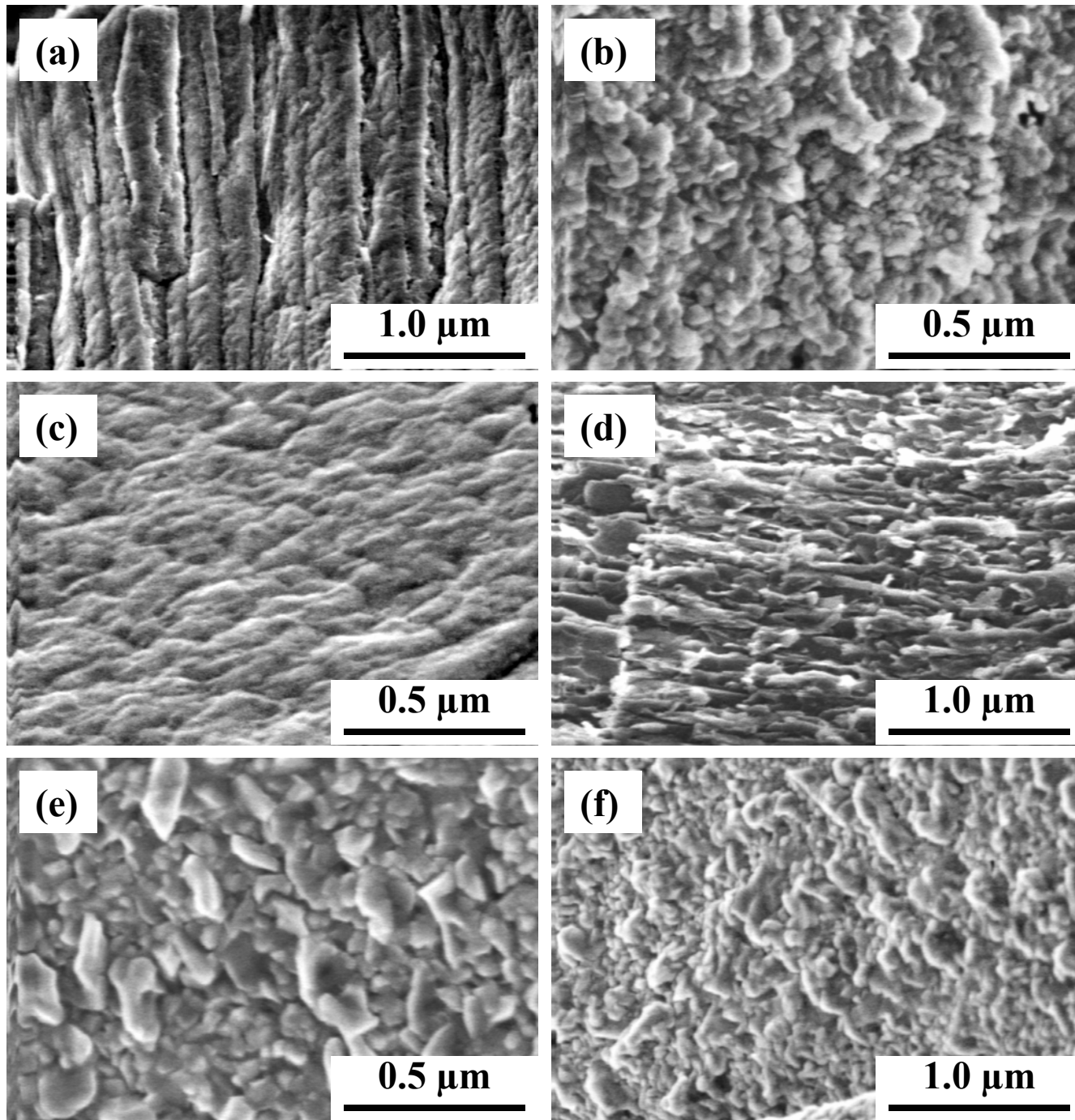


Fig. 7

1: LiD diffraction peaks

2: LiOH diffraction peaks

3: LiOH·H₂O diffraction peaks

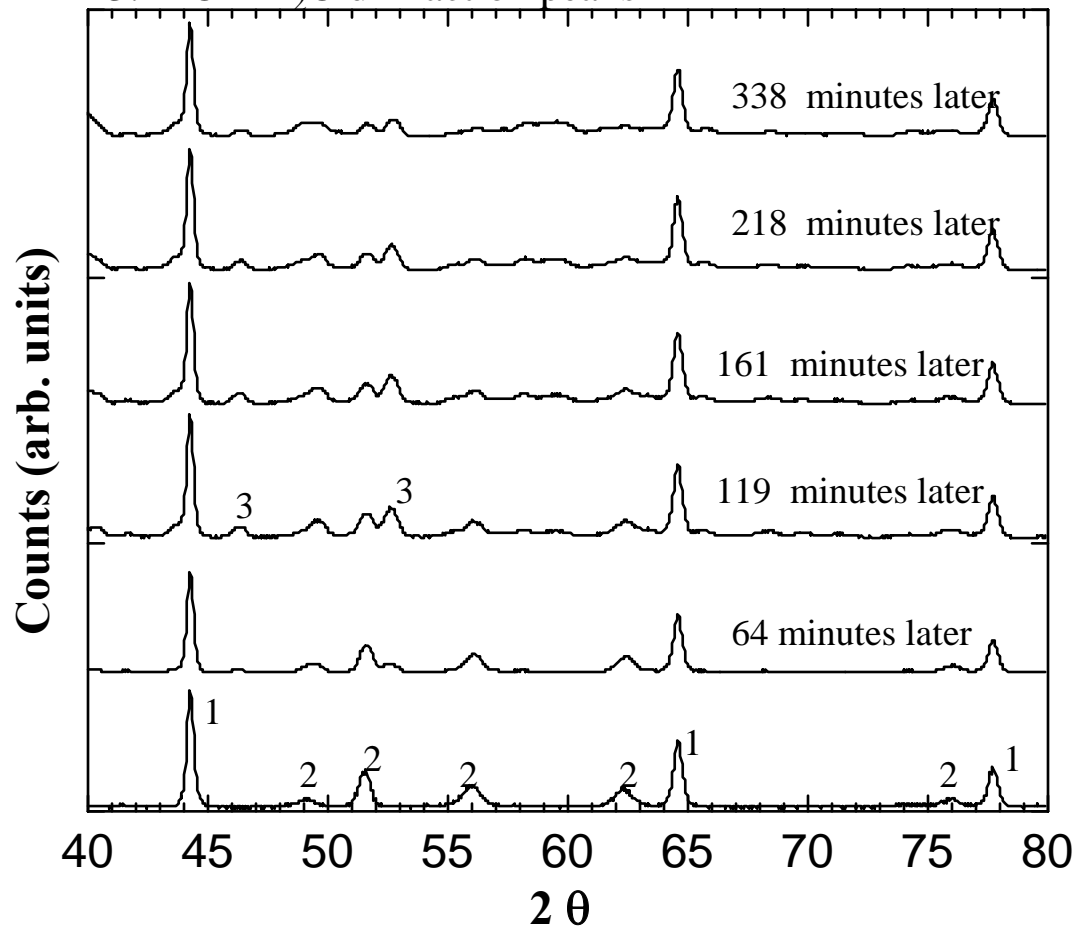


Fig. 8

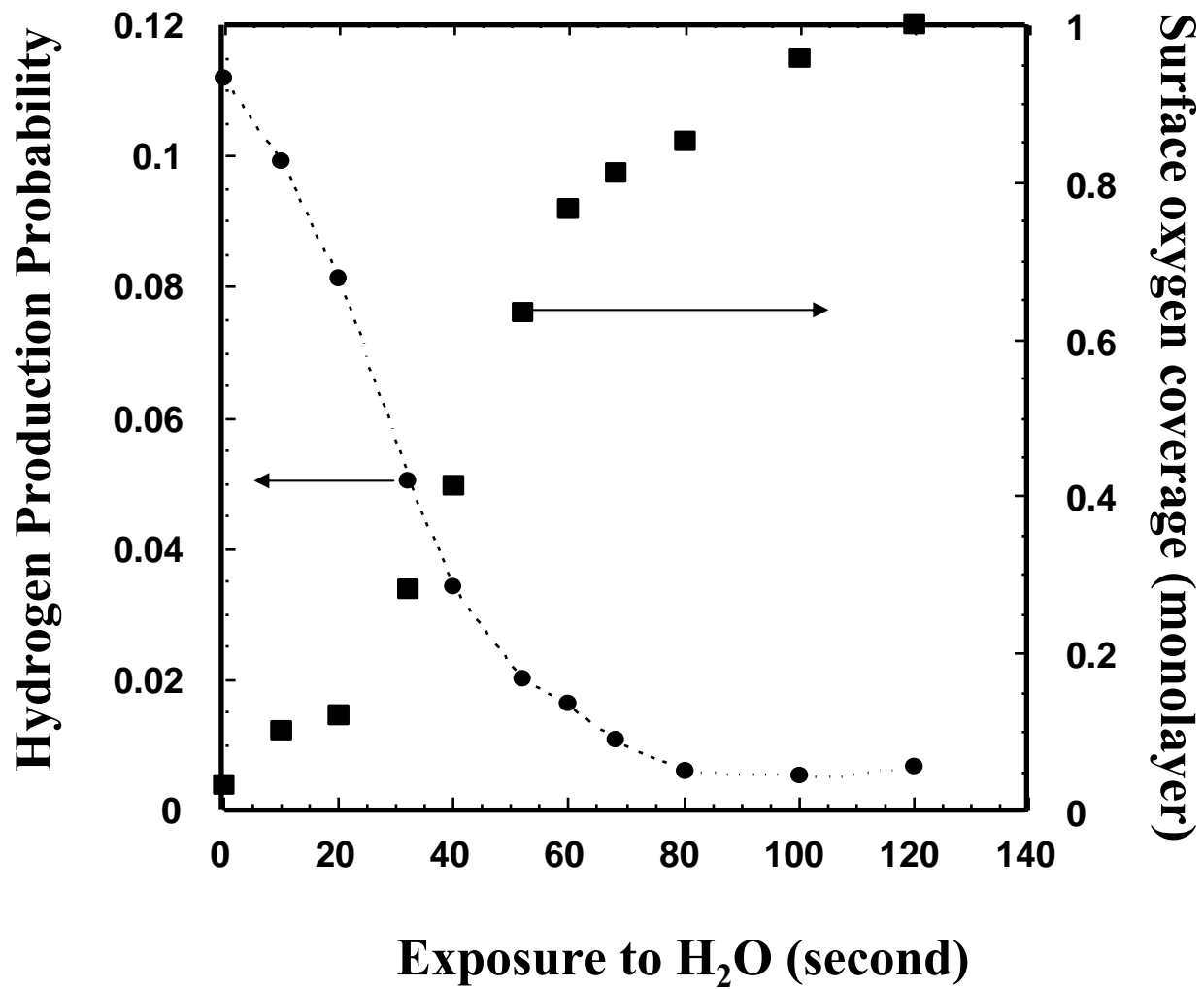


Fig. 9

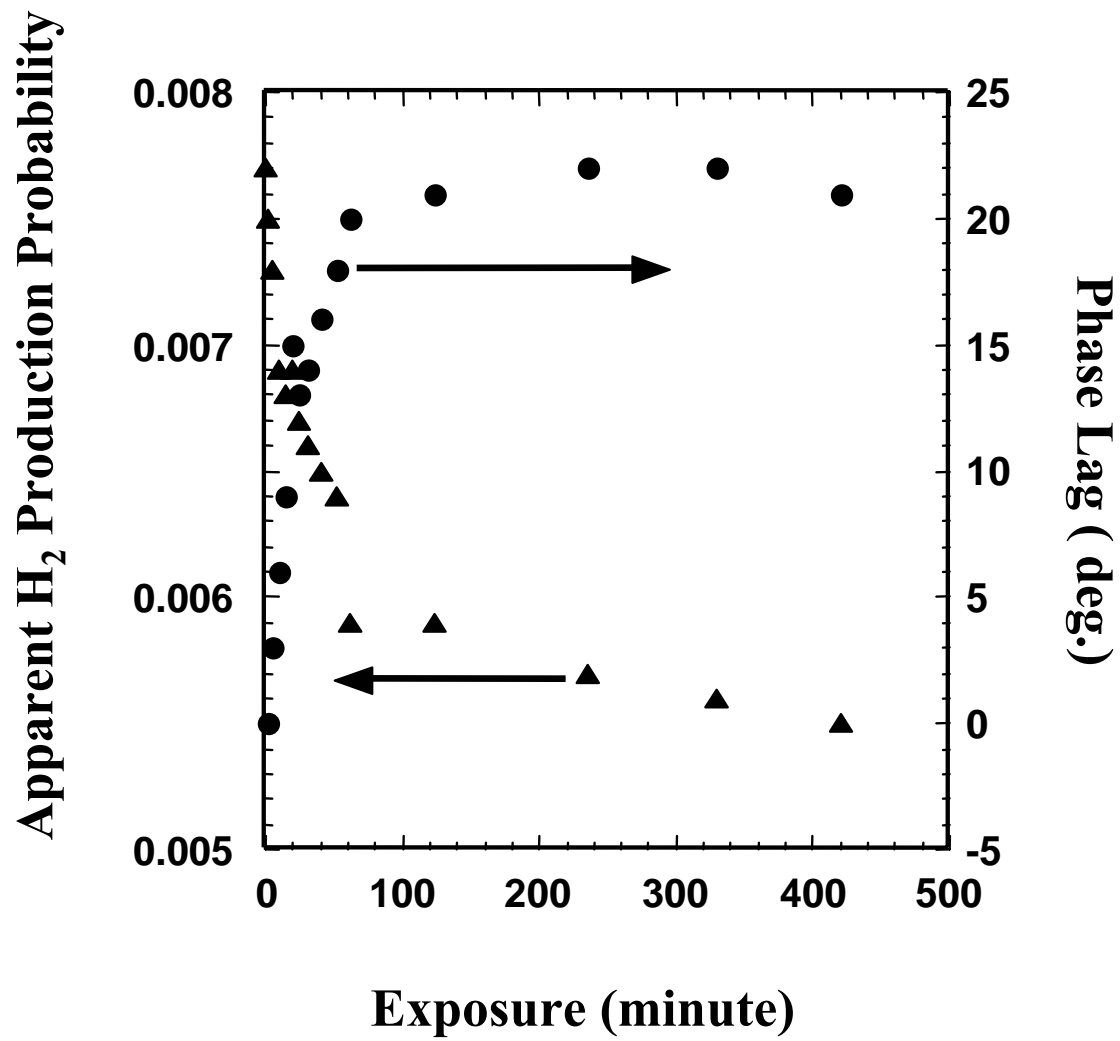


Fig. 10

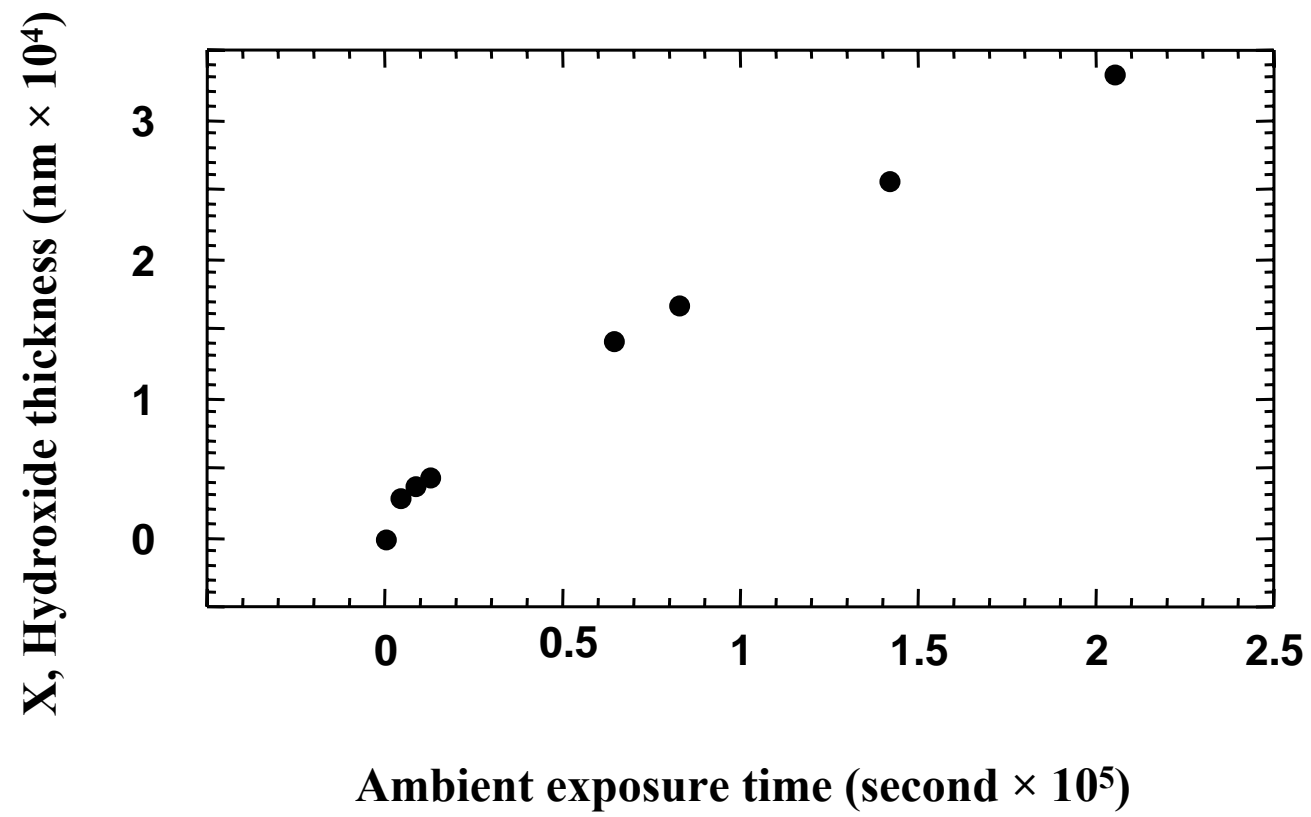
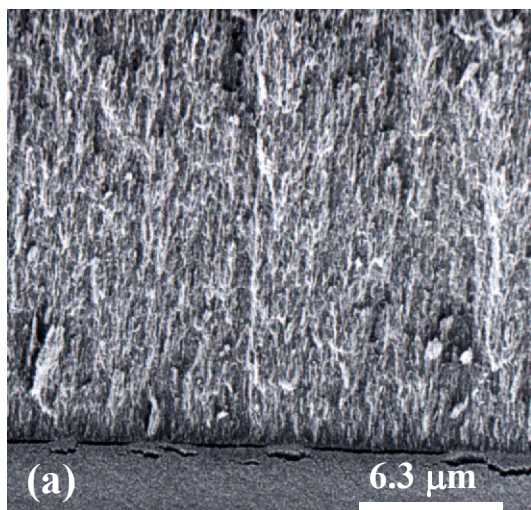


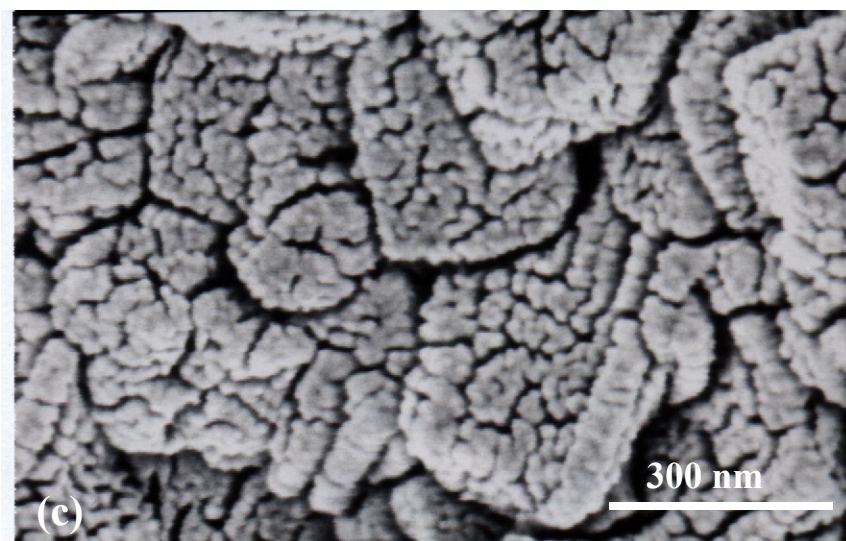
Fig. 11



LiOH grown on LiD



**Higher resolution image of
the LiOH corrosion layer**



Looking from the top-down onto the LiOH film

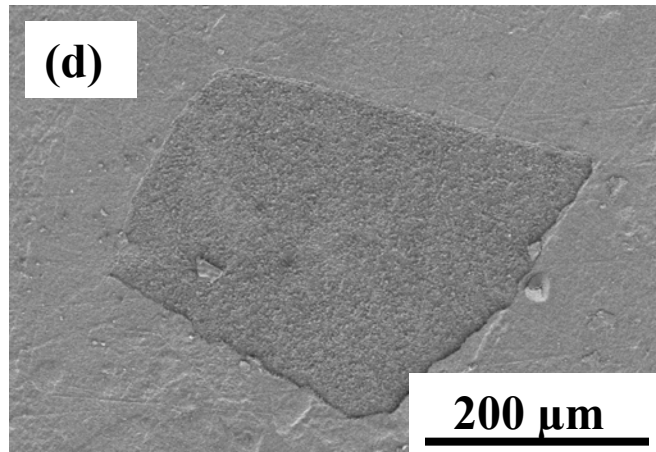
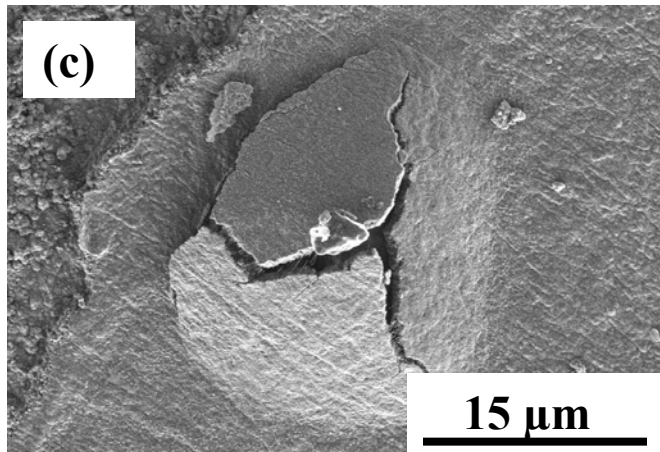
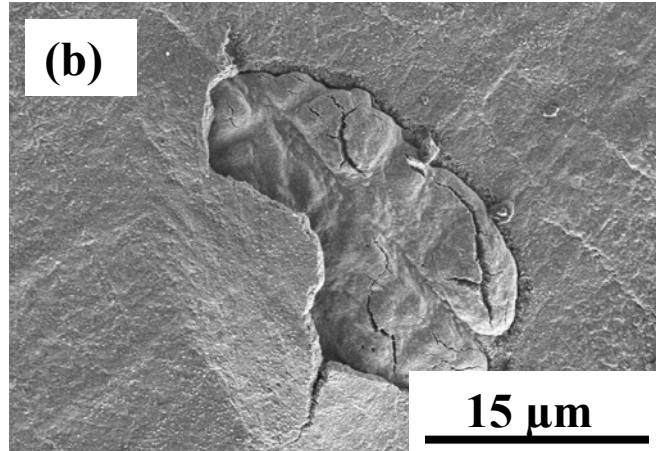
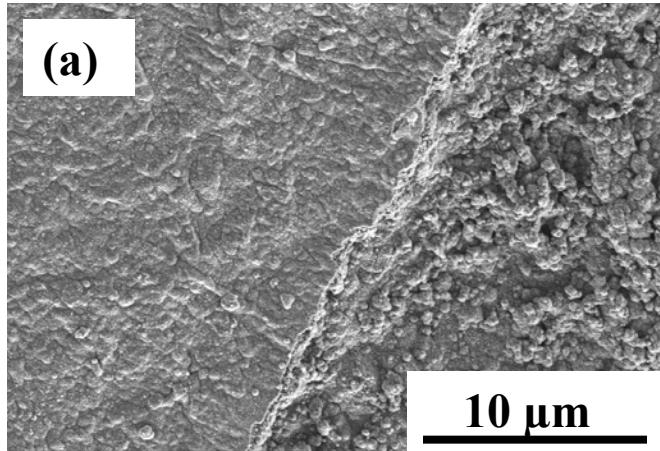
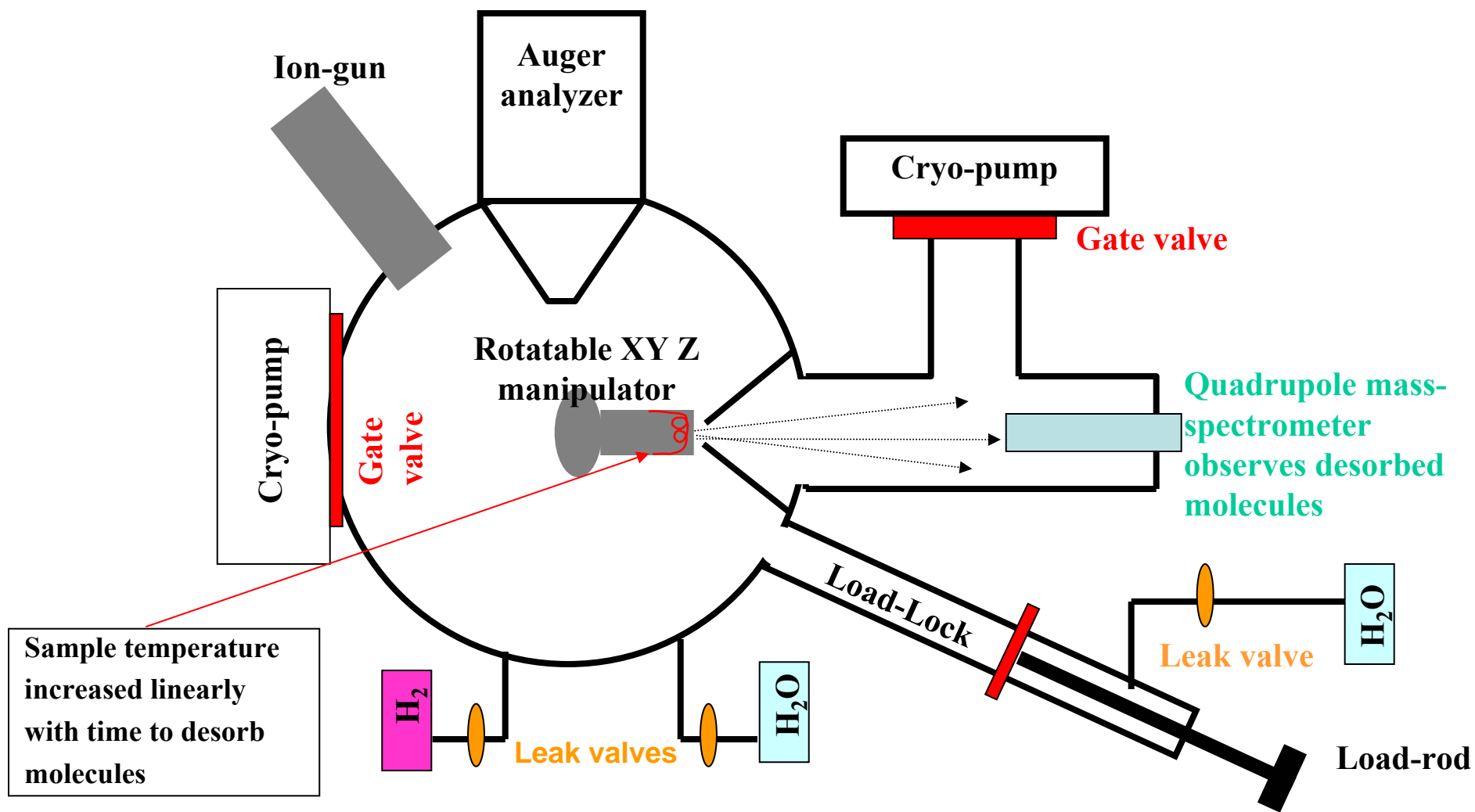


Fig. 13



Sample temperature
 increased linearly
 with time to desorb
 molecules

Fig. 14

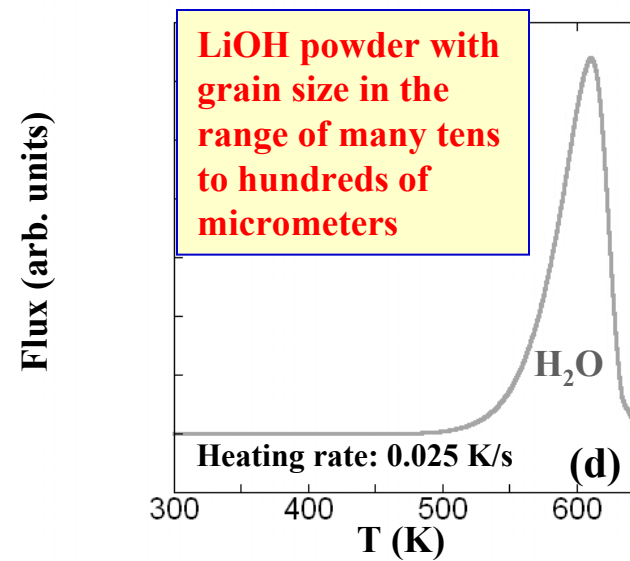
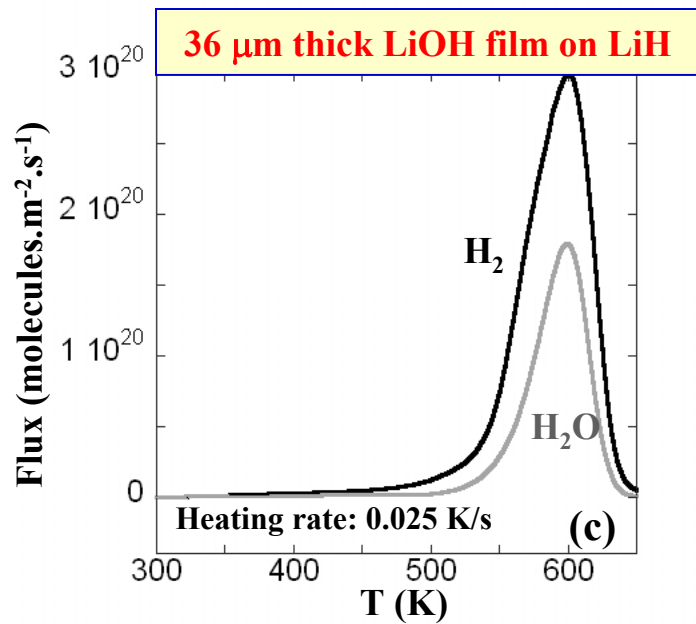
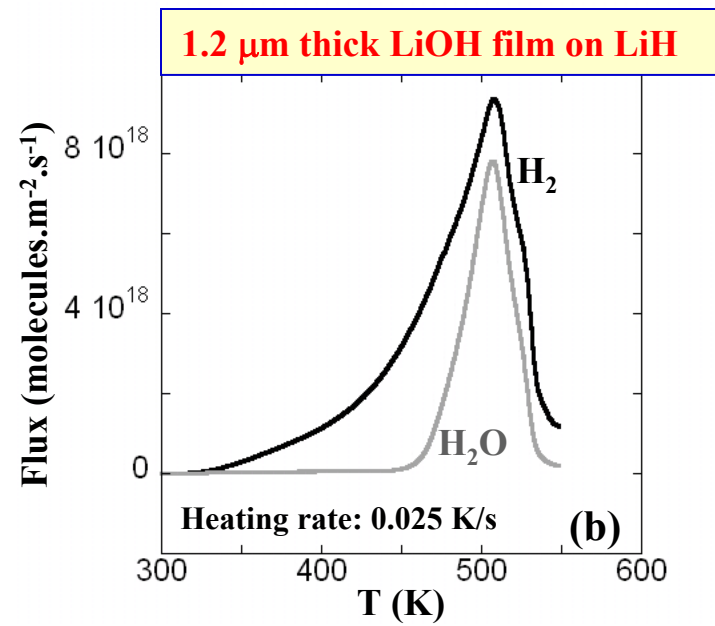
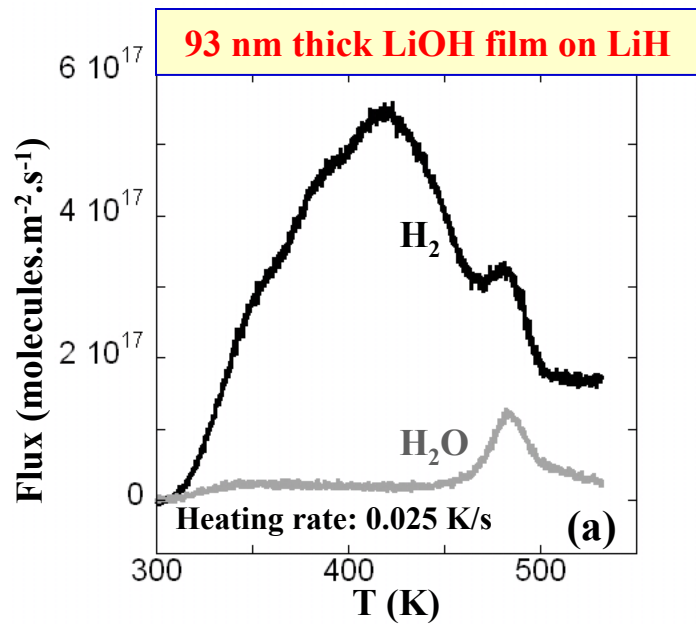


Fig. 15

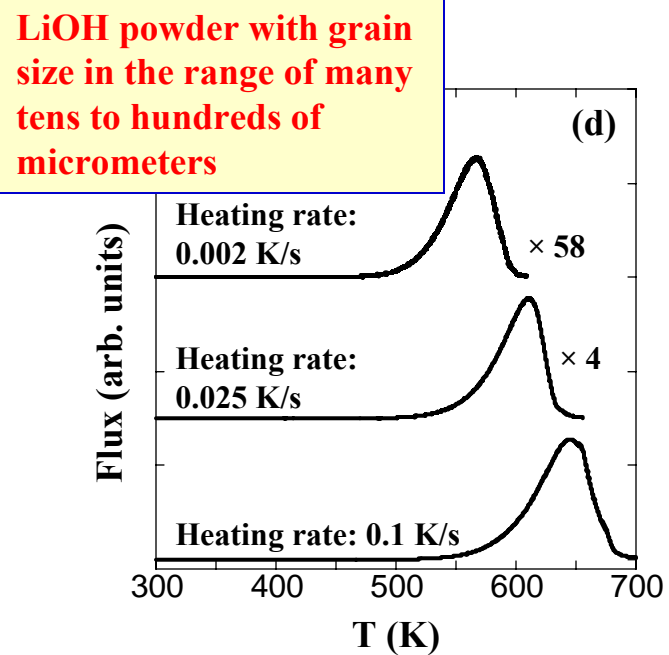
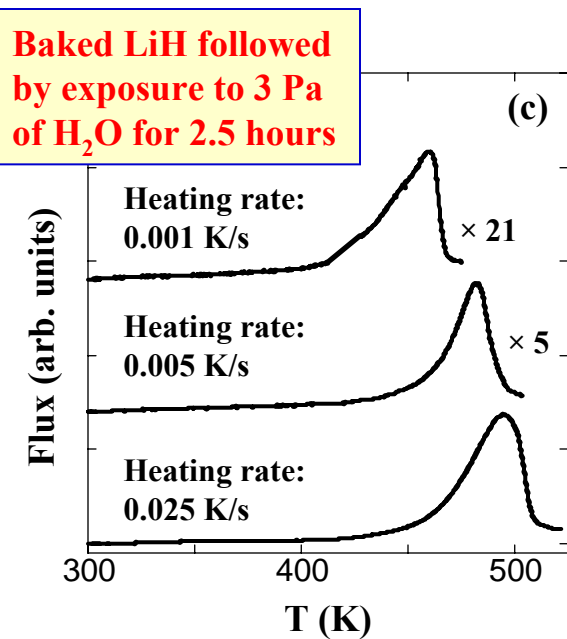
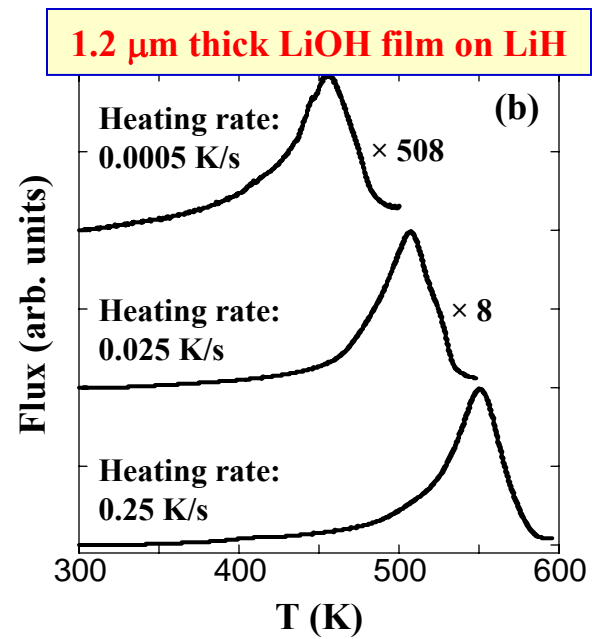
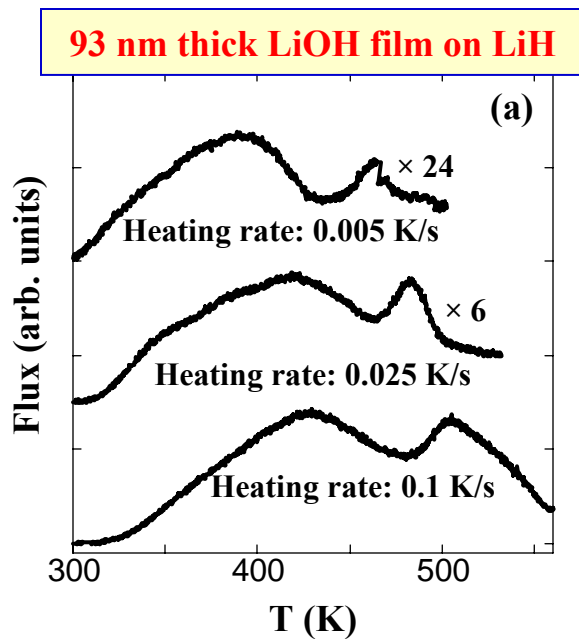


Fig. 16

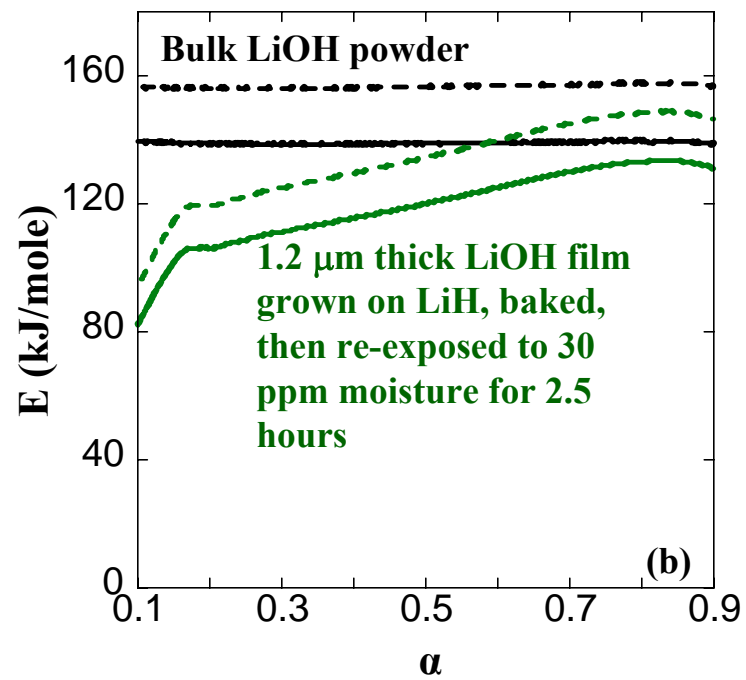
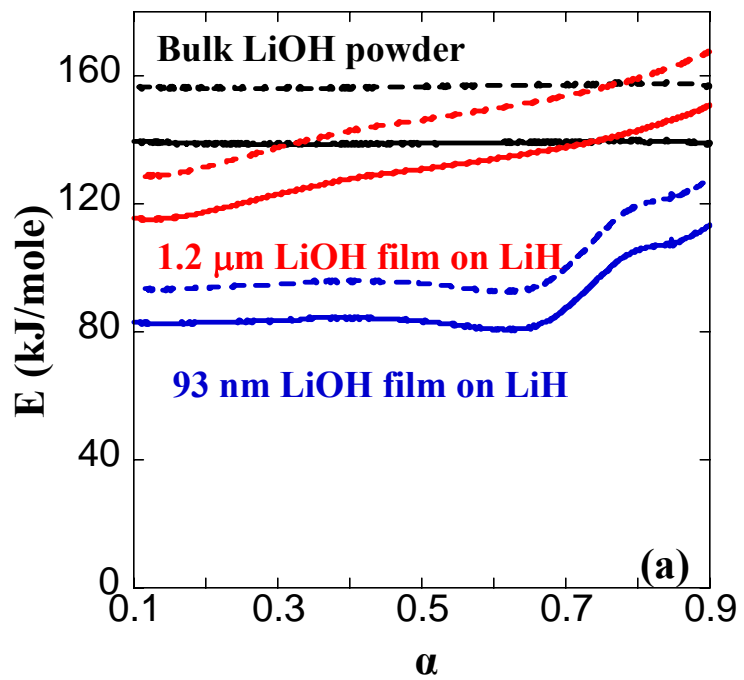


Fig. 17

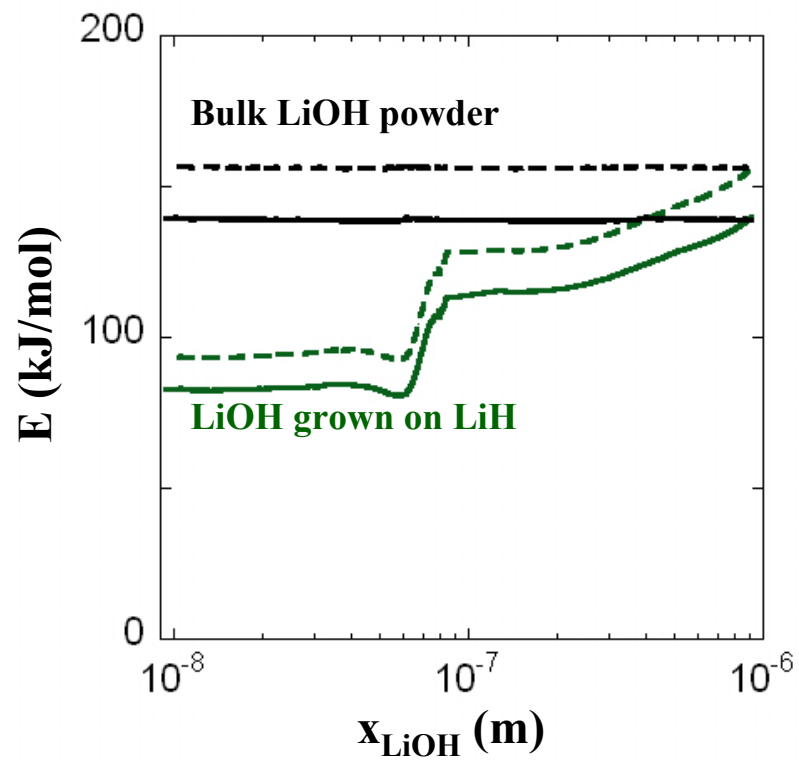


Fig. 18

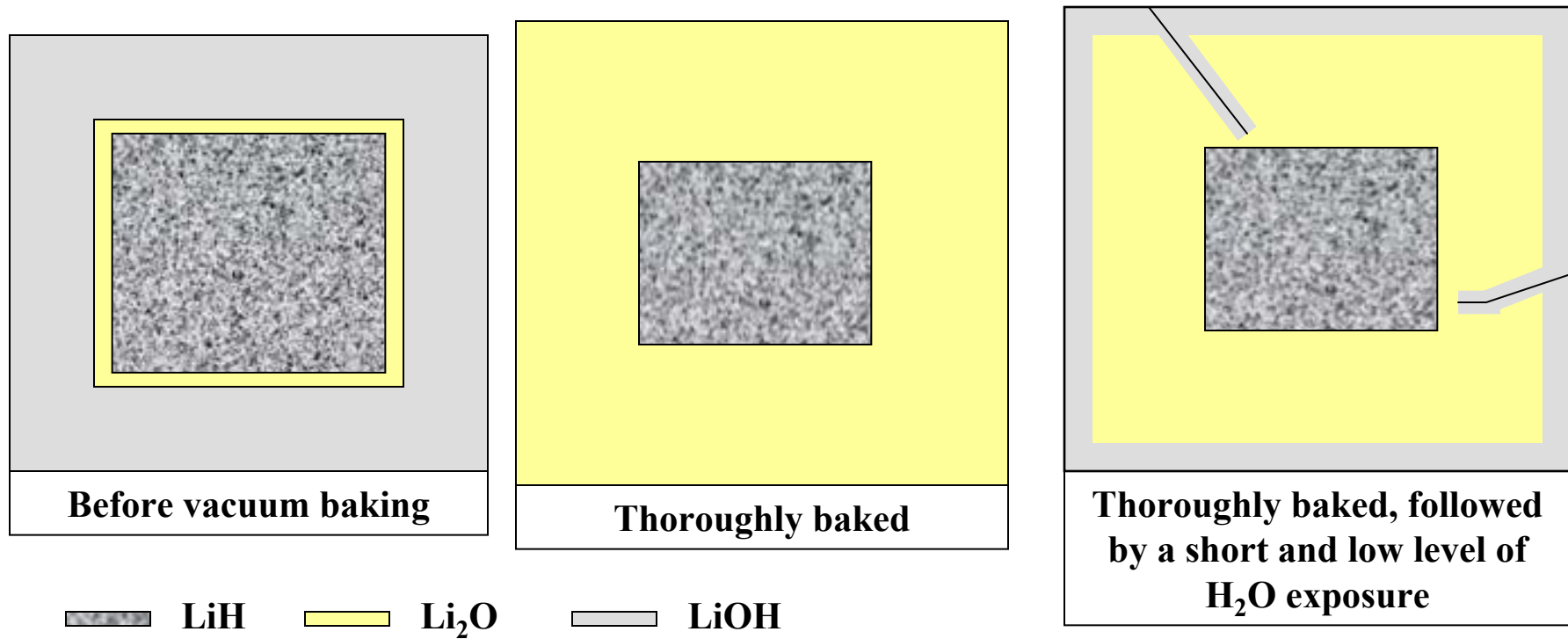


Fig. 19

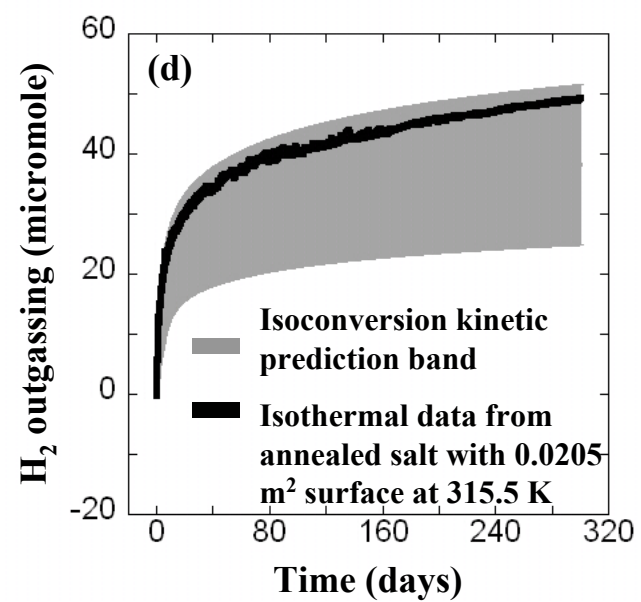
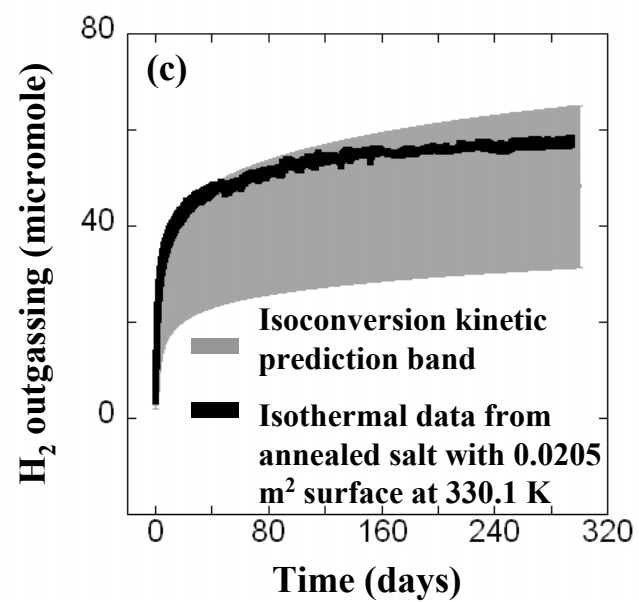
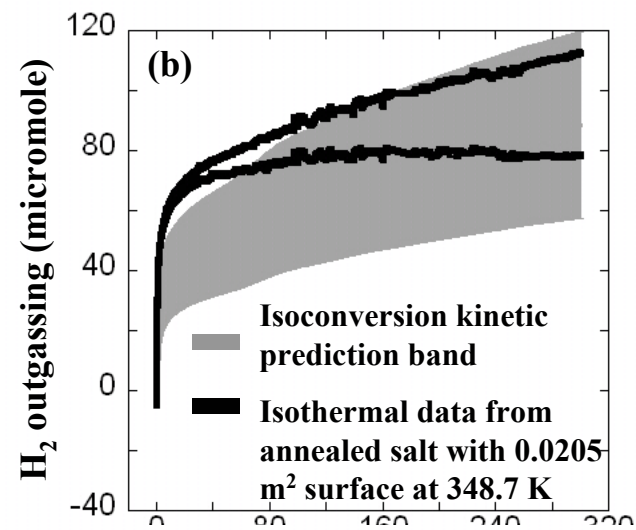
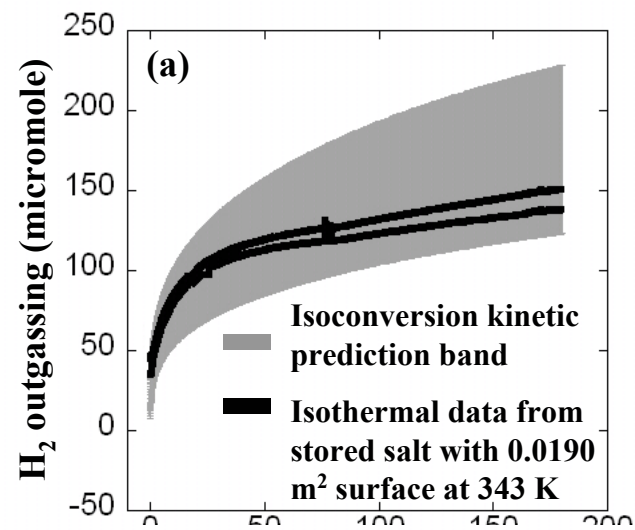


Fig. 20

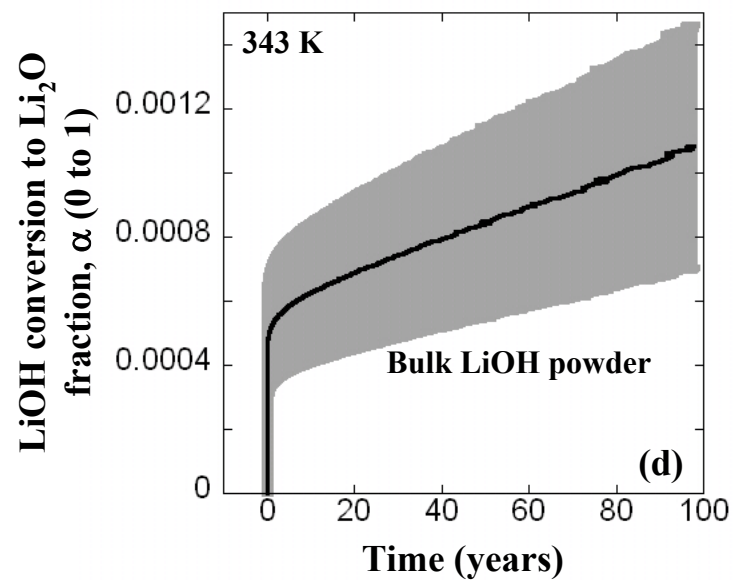
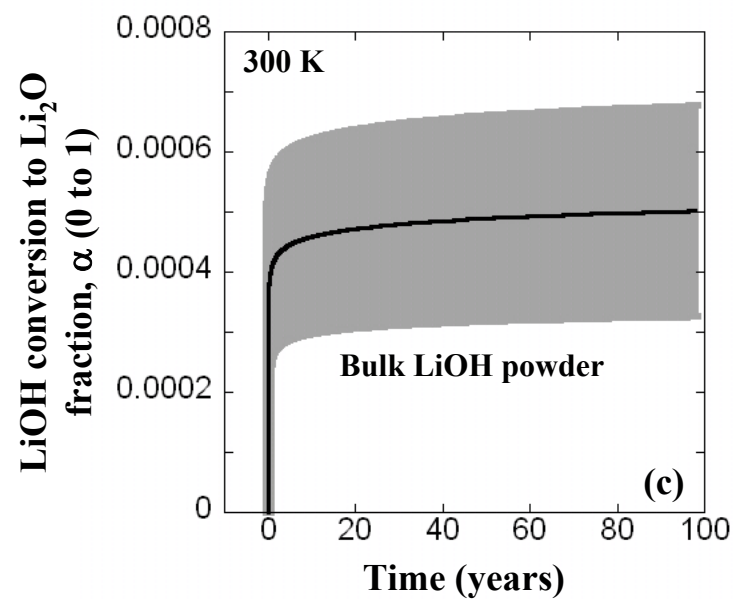
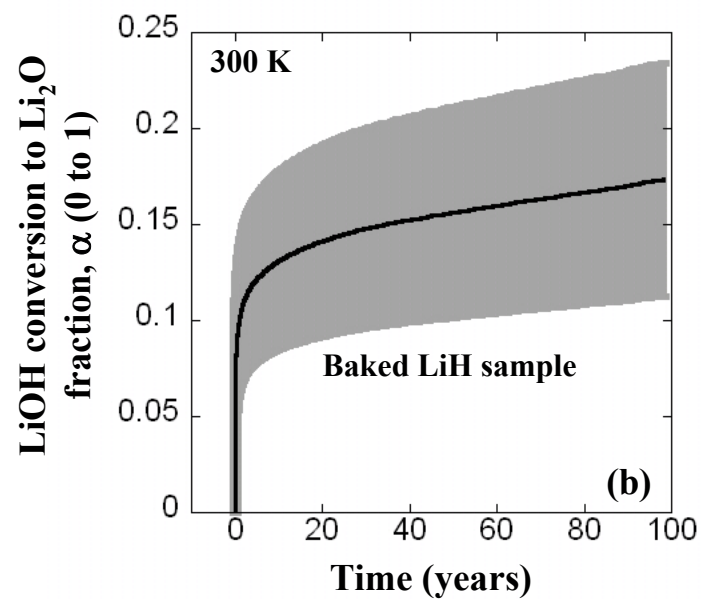
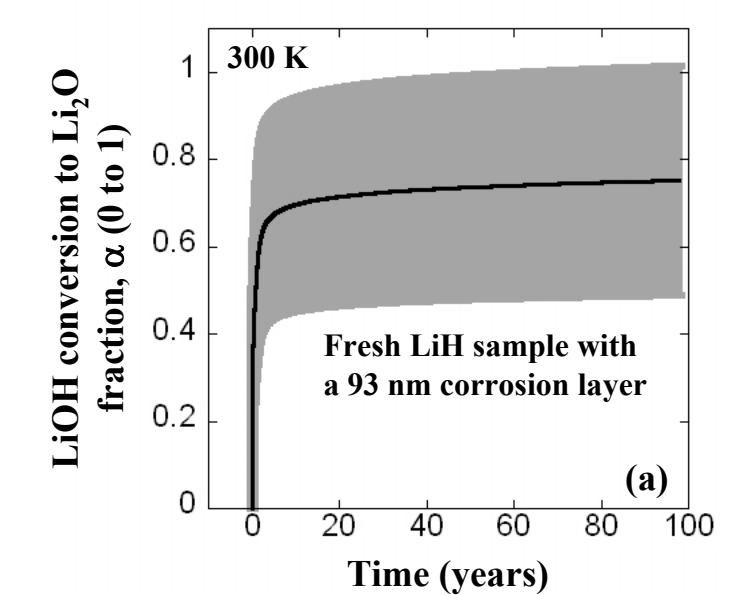


Fig. 21

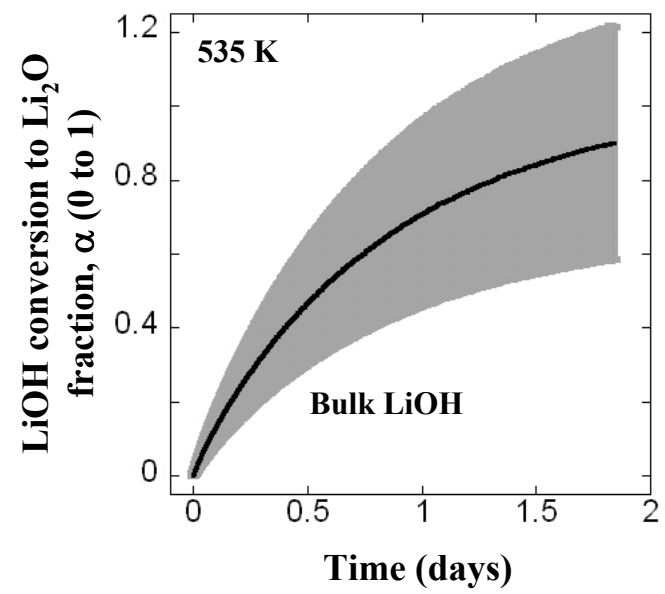


Fig. 22

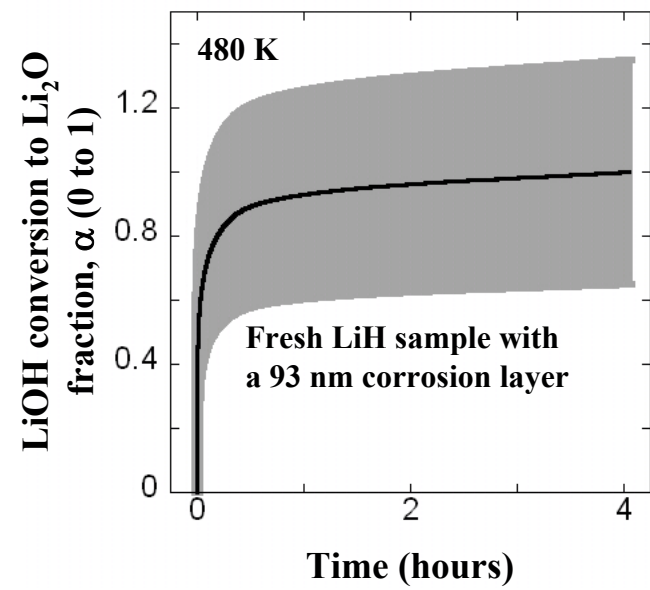


Fig. 23